Nascent dendrite branches initiated by a localized burst of Spire-dependent actin polymerization.

Authors: Deirdre Hatton[1,2,3,6], Claire Marquilly[1,2,6], Caitlin Hanrahan[1,2,3], Tiago Ferreira[1,2], Yimiao Ou[1,2], Lauren Cinq-Mars[1,2,3], Will Silkworth[4], Hannah M. Bailey[4], Margot E. Quinlan[4,5], Donald J. van Meyel[1,2*].

Affiliations: [1]Centre for Research in Neuroscience, Department of Neurology and Neurosurgery, McGill University, Montreal, Quebec, H3G 1A4, Canada.

[2]Research Institute of the McGill University Health Centre, Montreal, Quebec, H3G 1A4 Canada

[3]Integrated Program in Neuroscience, McGill University, Montreal, Quebec, H3A 2B4, Canada

[4] Dept. of Chemistry and Biochemistry, University of California Los Angeles, Los Angeles, CA, 90095, USA.

[5]Molecular Biology Institute, University of California Los Angeles, 607 Charles E. Young Drive, Los Angeles, CA 90095, USA

[6] These authors contributed equally.

***Correspondence**: don.vanmeyel@mcgill.ca

Summary

Dendrites form arbors whose size, shape and complexity define how neurons cover their receptive territories. Actin dynamics contribute to growth and remodeling of dendrite arbors. Here we examined how Spire, a conserved actin nucleation factor, promotes formation of new branches in vivo. In live imaging of Drosophila class IV dendritic arborization (c4da) neurons, Spire was observed at new sites of branch initiation, where it assembled new actin polymer in a burst just prior to filopodial outgrowth. For dendrite arborization, Spire required intact structural domains to nucleate actin and target the secretory network, and interacted with Rab11 GTPase, a key regulator of recycling endosomes. Together, these findings support a model in which Spire cooperates with Rab11 to promote new dendrite branches by linking localized actin dynamics with intracellular trafficking of endosomes that deliver lipids and cargoes to fuel protrusive outgrowth of nascent dendrites.

Introduction

Dendrites have distinct tree-like branching patterns that influence the number, strength, and integration of sensory or synaptic inputs into neurons[1-3]. Understanding how dendrites are shaped during development is essential to gain full insight into the construction of neural circuits that underlie animal survival, behaviors, learning, and memory[4]. A major gap remains in our understanding of the spatial and temporal control of cytoskeletal remodeling responsible for dendrite morphogenesis during development[5], though it is known to involve regulation of actin dynamics[6] by specific proteins to nucleate, elongate and remodel actin filaments[7,8]. Furthermore, to cope with their size and complexity, dendrites have specialized arrangements of secretory network organelles for the biogenesis of cargo-carrying vesicles and their transport to the cell surface[9]. Given the importance of actin and the secretory network for dendrite

development and function, it is important to clarify how they are coordinated to initiate new dendrite branches in vivo[5,10].

New dendrite branches arise from actin-rich filopodia that rapidly extend from initiation sites along established branches[10]. Dendrite filopodia are structurally distinct from conventional filopodia, with an unusual network-like cytoskeletal organization characterized by both branched and linear filaments of mixed polarity[11], suggesting involvement of multiple actin regulatory proteins with distinct activities. Few studies have identified specific actin regulators involved in forming new branches[12-17], and none have pinpointed their regulation of actin to the location and timing of nascent branch outgrowth. In Drosophila larvae, dendritic arborization (da) neurons provide an excellent model to study the roles of actin regulators in the development of dendrite arbors in vivo[18-20]. In da neurons, the locations of dendrite filopodia initiation sites are pre-figured by patches of actin polymer[12,16,21], as has been proposed for dendrite filopodia in the mouse brain also[22]. For the large space-filling arbors of class IV da (c4da) neurons, the formation of new dendrites requires the Arp2/3 actin nucleator complex under control of the activator WAVE and the small GTPase Rac1[12]. In c4da neurons, new dendrite formation also involves F-actin severing by Twinstar/Cofilin in the production of "blobs" of pre-assembled actin polymer, which move bidirectionally within dendrites, pause before filopodium outgrowth, and appear to contribute F-actin into the nascent branch[16]. The factors specifying the location and timing of filopodial outgrowth from actin patches and blobs have not been defined.

Here we explored the role of Spire (Spir), a conserved multi-domain actin nucleation factor. We previously showed that knockdown of Spir with RNA interference (RNAi) in cd4da neurons reduced the number of terminal dendrite branches and compromised the ability of these nociceptive neurons to elicit larval escape from noxious stimulus[23]. Spir is known to co-operate with Fmn-family formins, which are also actin nucleators, during Drosophila and mouse

oogenesis. Spir has four WASP homology 2 (WH2)-domains for actin nucleation, a KIND domain for interaction with Fmn-family formins[24-27], a modified FYVE (mFYVE) domain to target vesicles of the secretory network, and a SPIR-box with potential to interact with Rab GTPases[24,28-31], which play roles in vesicle sorting and transport[32,33]. Previous studies showed functional links between Spir and Rab11 in oocytes, in cultured cells, and in vitro[28,31,34,35], and Rab11 has been shown to be required for correct dendrite arborization of c4da neurons[36-38]. Here we show that Spir stimulates a burst of localized actin polymerization just prior to filopodial outgrowth of new dendrite branches and that Spir cooperates with Rab11 for dendrite arborization. Our data supports a model in which Spir and Rab11 link localized actin assembly with the secretory network to deliver lipids and cargoes to nascent dendrites.

Results

Spir is required in c4da neurons for localized F-actin synthesis just prior to outgrowth of new dendrite branches.

Development of Drosophila c4da dendrites begins in embryogenesis and continues in larval stages, with arbors growing in the larval body wall between muscles and epithelial cells[18]. We produced a *GAL4* line inserted in the *spir* locus (*spir*^{GAL4}) and used it to drive the reporter *UAS-mCD8::GFP*. *spir*^{GAL4} was expressed in c4da neurons (marked by ppk-CD4::tdTom) and other sensory neurons in the larval body wall (Fig. 1A), consistent with our previous report[23]. To examine Spir protein expression within c4da neurons, we developed new anti-Spir sera for immunohistochemistry (IHC) (Fig. S1A), and we also introduced an in-frame epitope-tag (smGFP-HA) into the *spir* locus (Fig. S1C, D). Both approaches showed Spir to be expressed in c4da neurons in third instar (L3) larvae.

73 To reveal actin dynamics leading up to the protrusion of dendrite filopodia, we acquired
74 time-lapse movies in second instar (L2) larvae, capturing F-actin (labeled with LifeAct::GFP)
75 within c4da neurons (labeled with ppk-CD4::tdTom). To study how loss of *spir* affects actin
76 accumulation and new branch initiation in c4da neurons, we used the mutant alleles $spir^{1}$ and
77 $spir^{2F}$, which prematurely truncate Spir within the KIND domain (Fig. 1B)[39]. We examined
78 each allele in combination with a deficiency for *spir* ($spir^{Df}$), which has a distinct genetic
79 background. All heteroallelic combinations of these alleles of *spir* are viable, and so with anti-
80 Spir sera we were able to confirm that *spir* mutants lack Spir expression in larval sensory
81 neurons (Fig. S1B), and adult brain lysates (Fig. S1G).

82 We captured movies of developing c4da dendrites in L2 larvae and mapped the
83 appearances of new branches in control animals heterozygous for $spir^{Df}$ (Fig. 1C, D) or $spir^{2F}$/+
84 (Fig. 1F), or in wild-type (+/+, Fig. 1F). In all of these controls LifeAct::GFP was seen in
85 stationary puncta that appeared prior to branch initiation; in wild-type (+/+) approximately half
86 of these puncta appeared *de novo* (Fig. 1C, F) and the other half were pre-formed actin blobs
87 that moved to the site (Fig. 1D), consistent with a previous report[16]. In $spir^{2F}/spir^{Df}$ mutants,
88 however, new branches arose only from pre-formed actin blobs that moved to the initiation site
89 and not from stationary actin puncta produced *de novo* (Fig. 1E, F).

90 In controls where branches initiated from either blobs or stationary puncta,
91 LifeAct::GFP signal at these sites became more intense just prior to branch initiation and then
92 extended into the protruding nascent branchlet (Fig. 1C, D). We quantified this change of
93 intensity in wild-type (+/+) controls, where LifeAct::GFP increased roughly two-fold on
94 average in the 60s prior to outgrowth and remained at this intensity for ≥ 60s (Fig. 1G). In
95 contrast, in $spir^{2F}/spir^{Df}$ mutants the LifeAct::GFP signal in blobs did not increase prior to
96 branch initiation (Fig. 1E, G), indicating that Spir is required for this localized assembly of F-
97 actin just prior to the outgrowth of new dendrite branches.

98

99 **Localization of Spir at nascent branches.**

100 In c4da dendrites, Spir was observed in puncta in dendrite branches near the cell body,
101 but strong labelling from epithelial cells and muscles prevented their detection and
102 quantification in more distal branches (Fig. S1A, C, D). To overcome this, we expressed a
103 *UAS-Spir::GFP* transgene (Fig. 1B) in c4da neurons with *ppk-GAL4,* and characterized the
104 distribution of Spir::GFP (Fig. S1E). In L3 larvae, GFP-labeled puncta were seen in 100% of
105 shafts, 28% of branch points, and 6% of branch tips (Fig. S1F). Consistent with this, most of
106 these GFP-labeled puncta were found along shafts (57%) or at branch points (36%) (Fig. S1F).

107 We next used live imaging to determine if Spir::GFP localized to sites of new branch
108 initiation in L2 larvae. Movies (~1 frame/2 seconds (sec) for >5 minutes (min)) showed a
109 distribution of Spir::GFP (Fig. 2A, B) similar to that of fixed larvae at L3 (Fig. S1E). Some
110 puncta were stationary while others were steadily motile or moved in a saltatory manner with
111 occasional pauses (Fig. S1H). Motile puncta were often smaller and rounder, while stationary
112 puncta were often larger and irregular in shape. Importantly, every nascent branch in controls
113 (+/+, L2) had a punctum stationed precisely at (68%) or near (< 2 μm, 32%) the initiation site
114 prior to outgrowth (Fig. 2C). These puncta arrived from elsewhere (30%, Fig. 2A, D) or were
115 already at that site in the first frame (70%, Fig. 2B, D), and time until branch outgrowth varied
116 (Fig. 2D). Spir::GFP intensity did not typically increase prior to outgrowth but, in some
117 instances (12%), a motile punctum combined with one already stationed at the future initiation
118 site. Spir::GFP at branch initiation sites was stably maintained throughout the process of
119 filopodial outgrowth, stabilization, or retraction, and invaded the filopodia as they grew (Fig.
120 2B).

121

122 **Spir is required for new branch formation.**

123 At the outset of our timelapse movies, the number of terminal dendrites/μm^2 was
124 reduced in *spir*^{2F}/*spir*^{Df} mutants compared to controls and, importantly, so was the number of
125 new branches/μm^2 formed per min during each movie (Fig. 2E). This was also observed in
126 movies of c4da neurons expressing LifeAct::GFP instead of Spir::GFP (Fig. S2A, B). For new
127 branches, growth occurred by saltatory extensions in both controls and *spir*^{2F}/*spir*^{Df} mutants,
128 but there were no differences between them in mean speed of outgrowth, proportion of time
129 spent paused between extensions, or maximum length of protrusion (Fig. S2C-E). For pre-
130 existing branches, the proportion that were static increased in *spir*^{2F}/*spir*^{Df} mutants (Fig. S2F-
131 I), whether LifeAct::GFP was present or not. Together these results confirm that Spir promotes
132 the formation of new branches and contributes to dynamics of pre-existing ones.

133 Consistent with this, we examined the consequences of Spir function for fully formed
134 arbors of c4da neurons at L3 and found that *spir* mutants (*spir*^{1}/*spir*^{Df} or *spir*^{2F}/*spir*^{Df}) had fewer
135 terminal branches than controls (*spir*^{2F}/+) (Fig. 3A, C), and thus shorter total arbor length (Fig.
136 3D). Sholl analysis also showed reduced peaks of maximum branch density (critical value)
137 (Fig. 3B, F). Dendritic field was reduced in some c4da neurons of *spir*^{2F}/*spir*^{Df} mutants (Fig.
138 3E), and so we repeated the analysis after removing a subset (4/15) of cells with unusually
139 small dendritic fields. As expected, we found that dendritic field was no longer significantly
140 different from controls (Fig. S3A) but the branching deficits were still strongly evident for the
141 number of terminal dendrites, arbor length and critical value (Fig. S3A-D).

142 Importantly, the selective expression of *UAS-Spir::GFP* in c4da neurons with *ppk-*
143 *GAL4* (Fig. 3A) fully rescued number of terminal branches in *spir*^{2F}/*spir*^{Df} mutants (Fig. 3C,
144 and critical value (Fig. 3B, F, Fig. S3D), demonstrating that Spir acts within c4da neurons to
145 control these features. It did not fully rescue total arbor length (Fig. 3D, Fig S3C), which is not
146 likely to be due to inadequate expression since IHC (Fig. S1E) and western blots (Fig S1G)
147 showed Spir::GFP at higher levels than endogenous Spir. Perhaps additional cell types

148 contribute to total arbor length, such as epithelial cells in the larval body wall where Spir is
149 expressed (Fig. S1A-D). We conclude that Spir acts within c4da neurons to establish the correct
150 number of terminal branches, likely by contributing to filopodial outgrowth necessary for
151 nascent branches.
152
153 **Each domain of Spir is required for dendrite arborization.**
154 We sought to determine the importance of the four identified protein domains of Spir
155 by testing if disruptive mutations in Spir::GFP (Fig. 1B) could rescue the correct numbers of
156 terminal branches in c4da neurons of *spir* mutants. The Y232K mutation is a missense
157 substitution in the KIND domain known to abolish the interaction between Spir and the Fmn-
158 family formin Cappuccino (Capu) in oocytes[25,40]. The ABCD mutation is a series of 4 triple-
159 alanine substitutions in the WH2 domains that greatly diminish the ability of Spir to polymerize
160 F-actin *in vitro*[24]. The ΔSB mutation is a 20 aa deletion of the entire Spir-box domain which
161 has sequence similarity to the Rab effector protein Rabphilin3a suggesting it interacts with Rab
162 GTPases[28]. Finally, the C5,6S mutation involves substitution of serine residues for 2 key
163 cysteines in the so-called modified FYVE (mFYVE) domain. FYVE domains interact in lipid
164 membranes with Phosphatidylinositol 3-phosphate (PtdIns3P), a prominent component of the
165 membranes in the endosomal system[41]. The mFYVE domain in Spir binds less specifically to
166 negatively charged lipids, including PtdIns3P, and is required for Spir's localization to
167 intracellular membranes[29].
168 When expressed in c4da neurons (with *ppk-GAL4)* of $spir^{2F}/spir^{Df}$ mutants, none of
169 these mutations rescued the number of terminal dendrites per neuron (Fig. 4A) or critical value
170 (Fig. 4B, Fig. S4A). This was not due to insufficient supply because none were expressed at
171 lower levels than intact Spir::GFP in western blots of adult head lysates (Fig. 4C, D and Fig.
172 S4B). The Y232K, ABCD, and C5,6S mutations did not obviously affect the punctate

173 distribution of Spir::GFP in static images of c4da arbors in L3 larvae (Fig. S4C), but the ΔSB
174 mutation caused it to accumulate near the cell soma and form a more continuous pattern (Fig.
175 4E). Though this might be explained in part by unusually high expression levels (Fig. 4C, D
176 and Fig. S4B), these results suggest that the SB domain is required for proper localization of
177 Spir within c4da arbors. None of the mutants appear to have dominant-negative activity, since
178 expression in a wild-type (+/+) background caused no significant differences in number of
179 terminal dendrites or total arbor length compared to Spir::GFP (Fig. S5A-E), though the ΔSB
180 mutation trended toward reductions of both parameters. Based on the failure of these four
181 mutations to rescue $spir^{2F}/spir^{Df}$ mutants, we conclude that each domain of Spir contributes to
182 its control of dendrite branching.
183
184 **Spir and Rab11 cooperate for dendrite arborization.**
185 The pattern and motility of Spir::GFP puncta within dendrites of c4da neurons was
186 reminiscent of elements of the secretory network, where Rab GTPases including Rab11 are
187 key regulators of vesicle and cargo trafficking[32]. Rab11 is associated with the trans-Golgi
188 network, post-Golgi, and recycling endosomes[42]. Rab11 has been shown to be required for
189 correct c4da dendrite arborization[36-38], a finding we confirmed with RNAi knockdown of
190 *Rab11* mRNA in c4da neurons (Fig. 5A) which reduced the numbers of terminal dendrites in
191 L3 larvae (Fig. 5B), total arbor length (Fig. 5C), dendritic field (Fig. 5D), and Sholl critical
192 value (Fig. 5E, F) compared to controls (+/+).
193 Whether Rab11 is involved in the initiation of new dendrite branches has not been
194 determined. To address this, we mapped the appearance of new branches in movies (~1 frame/2
195 sec for >5 min) of developing c4da dendrites in L2 larvae (Fig. 5G). In controls (+/+, L2) we
196 observed Rab11::GFP at (60%) or near (< 3 μm, 40%) the initiation site of each new dendrite
197 branch (Fig. 5H). Rab11 puncta were motile within arbors but in all instances of nascent

198 branches we observed, Rab11::GFP was already stationed at the initiation site from the
199 beginning of every movie and so we could not determine how long Rab11::GFP had been there
200 prior to outgrowth. Consistent with our findings at L3, Rab11 knockdown also reduced the
201 total number of terminal branches/μm^2 at L2 (Fig. 5I). Importantly, Rab11 knockdown severely
202 reduced the number of new branches/μm^2/min in each movie (Fig. 5J), indicating that Rab11
203 is required for the initiation of new dendrite branches. As in *spir* mutants (Fig. S2F-I), pre-
204 existing branches were affected by Rab11 knockdown (Fig. S6A-D): the proportion of branches
205 that both extended and retracted was reduced (Fig. S6C), while the proportion of static branches
206 increased (Fig. S6D). Therefore, loss of Rab11 results in fewer new branches and reduced
207 dynamics of existing ones.

208 Overexpression of Rab11::GFP had little effect on dendrite arborization at L3, since
209 the number of terminal dendrites, arbor length, and Sholl critical value were unaffected (Fig.
210 S6E, F, H), though the dendritic field was smaller (Fig. S6G). Nor did overexpression of
211 Rab11::GFP affect the dynamics of pre-existing branches at L2 (Fig. S6A-D).

212 Since Rab11, like Spir, is required for proper dendrite arborization, is localized to sites
213 of new branch initiation, and is required for their formation, we wondered if Rab11 and Spir
214 were related in regulating these processes. We first asked whether expressing excess Spir::GFP
215 could restore dendrite arborization and new branch formation to neurons lacking Rab11 by
216 RNAi. We found that it could not (Fig. 5B-F, I, J), suggesting that Spir is not simply a
217 downstream effector of Rab11.

218 We next wondered whether Rab11 and Spir might interact with one another and,
219 consistent with this, we found that upon simultaneous expression of Rab11::mCherry and
220 Spir::GFP in c4da neurons, they co-labelled in puncta within dendrites (Fig. 6A). To test
221 whether Spir and Rab11 can physically associate with one another *in vivo*, Spir-tdTom was co-
222 expressed with either Rab11::GFP or Capu::GFP (a positive control) in all neurons using the

223 *nSyb-GAL4* driver. From lysates of adult heads, co-immunoprecipitation revealed that
224 Spir::tdTom associates with both Rab11::GFP and Capu::GFP (Fig. 6B), but not with Rab6-
225 GFP (negative control, data not shown). This suggests that Spir could selectively associate with
226 Rab11-containing protein complexes in neurons.

227 We next asked if Rab11 is required for the correct localization of Spir within dendrites
228 of c4da neurons. Upon Rab11 knockdown the punctate distribution of Spir::GFP appeared
229 unaffected at L3 (Fig. S7A, B), and also at L2 (Fig. S7C) when it was positioned at (56%) or
230 near (< 2 μm, 44%) the initiation site of each new dendrite branch (Fig. S7D). Together, these
231 results suggest that although Spir and Rab11 are found at many of the same locations within
232 dendrites, Rab11 is not required for Spir localization there.

233 Genetic interaction experiments that examine trans-heterozygotes for mutant alleles
234 *spir* and *Rab11* can provide evidence that they operate in a common molecular pathway. When
235 compared to control heterozygotes for either mutation alone (Fig. 6C) the c4da neurons of
236 trans-heterozygotes showed reduced numbers of terminal branches (Fig. 6D) and arbor length
237 (Fig. 6E), while dendritic field was largely unaffected (Fig. 6F). Together with their co-
238 localization in c4da neurons and their co-immunoprecipitation, this genetic interaction
239 provides strong evidence that Spir and Rab11 functionally interact with one another, either
240 directly or indirectly, in a common molecular pathway for dendrite arborization in c4da
241 neurons.

242

243 **Discussion**

244 Spir was identified previously as being regulated by Longitudinals Lacking (Lola), a
245 BTB/POZ transcription factor involved in dendrite development[23] and motor axon guidance[43].
246 However, the mechanisms of Spir function in neuronal development have remained unclear.
247 Our data presented here indicate that Spir stimulates localized assembly of actin in the seconds

248 prior to outgrowth of new dendrite branches, and that Spir function is linked to the GTPase
249 Rab11 in the formation of new branches and the dynamic motility of existing ones. Unlike
250 Spir::GFP which arrived from elsewhere in 30% of new branch initiation events, Rab11::GFP
251 was already at the site from the beginning of every movie, suggesting that, at least in some
252 cases Spir is recruited to a pre-existing site marked by the presence of Rab11. Rab11 has been
253 shown to regulate movement of recycling endosomes toward the plasma membrane[44], and the
254 trafficking of receptors and trans-membrane proteins necessary for neurite outgrowth and
255 remodelling[45,46]. We therefore propose that Spir cooperates with Rab11 to couple actin
256 dynamics with the delivery of lipids and cargoes through the secretory network to fuel
257 protrusive outgrowth of nascent dendrites. Consistent with this, Spir function in dendrite
258 arborization required intact domains for actin assembly (KIND, WH2) and for targeting Spir
259 to the secretory network (mFYVE). The Spir-box has potential to mediate interactions with
260 Rab GTPases, and we found that it was essential to control the levels and localization of Spir
261 in dendrites. However, knockdown of Rab11 alone did not dramatically alter the overall
262 punctate pattern of Spir::GFP, raising the possibility that additional Rabs or other factors are
263 involved in the localization of Spir within arbors.

264 In control animals, newly formed branches were pre-figured either by the appearance
265 of actin polymer *de novo* or by the arrival of pre-formed actin blobs, in roughly equal
266 proportions. In *spir* mutants, there were fewer new branches, and none stemming from
267 initiation sites with *de novo* actin polymer, indicating that Spir is critical for new dendrite
268 formation from such sites. It is unclear whether stationary actin patches and motile actin blobs
269 are features of convergent or parallel processes to initiate dendrite branches[47]. Although Spir
270 was present and active at initiation sites stemming from pre-formed actin blobs, it was
271 dispensable for branch initiation from at least some of them. From this we infer redundancy
272 with other molecular mechanisms for branch initiation, perhaps involving actin synthesized by

273 the Arp2/3 complex which has been shown to localize transiently to branch initiation sites in
274 c4da neurons[12].

275 Spir::GFP overexpression did not affect dendrite arborization (compare Fig. 3 and Fig.
276 S5), supporting the idea that its expression at nascent branch sites reflects that of endogenous
277 Spir. Since Spir::GFP overexpression was not sufficient to induce ectopic branching, and the
278 interval between stationing of Spir at a branching site and filopodial outgrowth was variable,
279 our findings suggest that Spir activity is tightly regulated and may require additional partners
280 to engage the switch to branch initiation. The KIND domain mutation Y232K is known to
281 abolish the interaction between Spir and the formin Capu, and there is some evidence that Spir
282 and Capu interact for the spike-like protrusions in dendrites of class 3 da neurons[17]. However,
283 in unpublished data we built a *capu*^{GAL4} line that did not label c4da neurons, and RNAi lines
284 targeting Capu did not reduce terminal branch number when expressed in c4da neurons. Of
285 note, the KIND domain also binds intramolecularly to the mFYVE domain[29], and so perhaps
286 the Y232K and C5,6S mutations in these domains disrupt this interaction and thereby impact
287 Spir function in dendrites. Alternatively, Spir might cooperate with another formin in c4da
288 neurons such as Formin3, which is required for c4da dendrite arborization[48]. Further research
289 will be required to identify a formin partner for Spir in c4da neurons, or to determine if Spir
290 could nucleate actin on its own in neurons, as has been shown *in vitro*[24].

291 Interestingly, the Formin3 ortholog INF2 has been reported to interact with mouse Spir-
292 1 in mammalian cells[49]. Murine orthologs of Spir (Spir-1 and Spir-2) are expressed in the
293 developing CNS and adult brain[50,51]. Decreased Spir-2 expression is associated with epilepsy
294 in humans and mice[52], but it is not known if either Spir-1 or Spir-2 are involved in dendrite
295 arborization in mammals. A distinct actin nucleator known as Cordon-bleu has been
296 demonstrated to promote dendrite branch initiation in cultured hippocampal neurons and slice
297 preparations of cerebellar Purkinje neurons[15].

298 Actin filaments generated by Spir proteins and formins have been shown to provide
299 tracks for myosin-V motors in microtubule-independent transport of Rab11-labeled endosomes
300 to the plasma membrane of oocytes[34,53] and in dispersal of Rab27a-labeled melanosomes in
301 melanocytes[54]. Interestingly, mammalian orthologs of myosin Vb have been shown to bind
302 directly to the orthologs of both Spir and Rab11[35], which together activate myosin Vb and
303 stimulate its motility[31]. In dendrites, Spir could contribute to an actin pool for myosin-V-
304 mediated delivery of Rab11 vesicles to nascent branches, supplying lipids and proteins required
305 for their protrusive growth. This actin pool could allow for the subsequent invasion of
306 microtubules into these nascent branches, perhaps mediated by myosin-6[55] or augmin[56], and
307 the transition to microtubule-dependent long-distance transport of cargo-carrying vesicles.
308 While further experiments are required to fully elucidate the mechanisms of dendrite
309 branching, our findings show that Spir-mediated actin dynamics link branch initiation with
310 protrusive outgrowth in vivo.
311

312 **Acknowledgements**

313 This work was supported by the Canadian Institutes of Health Research (FRN137034
314 to DJvM), National Institutes of Health (R01GM096133 to MEQ), a Ruth L. Kirschstein
315 National Research Service Award (GM007185 to HMB), and studentships from the RI-MUHC
316 and McGill (to DH). The authors thank Greg Emery, Peter McPherson and Martine Girard for
317 advice and sharing reagents, our colleagues Emilie Peco, Eunjoo Cho, Adela Ralbovska, Keith
318 Murai, Sabrina Chierzi and Todd Farmer for helpful suggestions. For technical support, the
319 authors thank Dr. Min Fu and Shi-bo Feng of the RI-MUHC Molecular Imaging Platform, and
320 Tim McLean. Stocks obtained from the Bloomington Drosophila Stock Center (NIH
321 P40OD018537) were used in this study.
322

323 **Author Contributions:**

324 D.J.v.M and M.E.Q. conceived the project and designed experiments with input from
325 all other authors. D.H., C.M., C.H., T.F., Y.O., L.C-M., W.S., and H.M.B. performed
326 experiments and analyzed all data. D.J.v.M wrote the manuscript with input from all other
327 authors.

328

329 **Declaration of Interests:**

330 The authors declare no competing interests.

331

332

333 **Figure Legends**

334 **Figure 1: Spir is required for localized F-actin synthesis just prior to new branch**
335 **outgrowth.** (A) *spir*^{GAL4}-driven mCD8::GFP in c4da neurons (ppk-CD4::tdTom) including
336 ddaC (arrowhead), and other sensory neurons in an L3 larva. Scale bar=25µm. (B) Diagram
337 showing Spir protein domains (KIND, WH2, SB, and mFYVE), the locations *spir*^{2F} and *spir*^{1}
338 mutations, and the names of the disruptive mutations (Y232K, ABCD, ΔSB, and C5,6S)
339 introduced into Spir::GFP. (C, D) Filmstrips (Supplemental Videos 1 and 2) of new dendrite
340 branch formation in a c4da neuron (ppk-CD4::tdTom) from a control (*spir*^{Df}/+) L2 larva.
341 LifeAct::GFP (driven by *ppk-GAL4*) reveals actin polymer within dendrites. Arrow (in C)
342 points to a punctum of F-actin appearing *de novo*, and arrowheads (in D) point to a pre-existing
343 punctum that moved from its original position (white arrowhead) to the site of branch initiation
344 (green arrowhead). In all instances, LifeAct::GFP signal intensified just prior to branch
345 initiation. Scale bar = 2µm. (E) Filmstrip (Supplemental Video 3) showing new dendrite branch
346 formation in a *spir*^{2F}/*spir*^{Df} larva at L2, where LifeAct::GFP moved to the initiation site but did
347 not intensify prior to outgrowth (arrow). Scale bar = 2µm. (F) Proportion of newly formed

348 terminal branches in L2 larvae that had either *de novo* F-actin or pre-formed F-actin prior to
349 branch initiation in c4da neurons. Graph shows mean ± SEM, comparing controls (+/+, n=50
350 new branches in movies from 11 neurons) with *spir* heterozygotes ($spir^{2F}$/+, n=18 new
351 branches, 8 movies) and *spir* mutants ($spir^{2F}/spir^{Df}$, n=8 new branches, 11 movies). (G) Fold
352 change of F-actin intensity (LifeAct:GFP) at branch initiation sites, from 60s before branch
353 formation to 60s afterward, comparing mean ± SEM of controls (black) and *spir* mutants (red).
354

355 **Figure 2: Spir is at initiation sites for new dendrite branches, and is required for their**
356 **formation.** (A, B) Filmstrips (Supplemental Video 5 and Supplemental Video 6) of control
357 (+/+) L2 larva, where Spir::GFP (arrows) was observed to move to the initiation site of a new
358 dendrite branch (A) or was already stationed there at the beginning of the movie (B). Scale bars
359 = 2μm. (C, D) For newly formed dendrite branches, the distance of the closest Spir::GFP puncta
360 from the site of branch initiation was measured (C), and the time from observation of a
361 stationary Spir::GFP punctum at the site to filopodial outgrowth was recorded (D). (E, F)
362 Dendrite parameters from time lapse movies of control (+/+, n=104 new branches, 10 movies),
363 heterozygotes ($spir^{2F}$/+, n=91 new branches, 10 movies) or $spir^{2F}/spir^{Df}$ mutants (n=42 new
364 branches, 15 movies). (E) Terminal branches/μm^2 in first movie frame (ANOVA
365 $F(2,32)=12.30$, $p<0.0001$). (F) Number of new branches/μm^2/min in each movie (ANOVA
366 $F(2,32) =9.276$, $p=0.0007$).
367

368 **Figure 3: Spir is required for dendrite arborization of c4da neurons.** (A) Dendrite arbors
369 in a *spir* heterozygote control (left), a *spir* mutant (middle), and a *spir* mutant rescued with
370 Spir::GFP (right). (B) Sholl profiles with dotted line indicating critical value for controls
371 ($spir^{2F/+}$). (C-F) Dendrite parameters per neuron in L3 larvae (n=15 for each genotype).
372 Asterisks indicate significant changes compared to $spir^{2F/+}$ heterozygous controls. (C) Total

373 number of terminal dendrites per neuron (ANOVA ($F(4, 70) = 11.30$, $p < 0.0001$). (D) Total
374 length of dendrite arbor (mm) (ANOVA $F(4, 70) = 15.12$, $p < 0.0001$). (E) Dendritic field
375 (mm^2) (ANOVA ($F(4, 70) = 3.352$, $p = 0.0144$). (F) Sholl critical value (ANOVA ($F(4, 70) =$
376 8.936, $p < 0.0001$).
377
378 **Figure 4: Structure-function analysis to identify Spir domains required for dendrite**
379 **arborization and Spir localization.** (A-B) Dendrite parameters (L3 larvae) showing rescue of
380 $spir^{2F}/spir^{Df}$ mutants with Spir::GFP, but failure to rescue by domain-specific mutations (n=15
381 for each genotype). (A) Total number of terminal dendrites per neuron (ANOVA ($F(5, 83) =$
382 2.269, $p = 0.0550$). (B) Sholl critical value (ANOVA ($F(5, 84) = 3.552$, $p = 0.058$). (C) Anti-
383 GFP and anti-Actin western blot analysis from adult head lysates, where transgenes were
384 expressed in all neurons with nSyb-GAL4. Expected size of Spir::GFP is 142 kDa, and
385 endogenous Actin is 42 kDa. (D) Relative band intensities on western blots (n=3) of Spir::GFP
386 constructs (anti-GFP) normalised to anti-Actin. $Spir^{\Delta SB}$::GFP is expressed at significantly
387 higher levels than Spir::GFP (Friedman test ($Q (4) = 10.40$, $p = 0.0053$), with Dunn's post-hoc
388 tests). (E) *ppk-GAL4*-driven Spir::GFP or $Spir^{\Delta SB}$::GFP in a *spir* mutant background. White
389 boxes in left panels indicate areas magnified in panels to their right. Scale bar=50µm. Spir::GFP
390 is punctate in dendrites, but $Spir^{\Delta SB}$::GFP accumulates in a continuous pattern in dendrites
391 proximal to the cell soma (white arrowhead).
392
393 **Figure 5. Rab11 is required in c4da neurons for dendrite arborization and new branch**
394 **formation.** (A) Dendrite arbors of c4da neurons in control (+/+) (left) and *ppk-Gal4*-driven
395 Rab11-RNAi (right) L3 larvae. Scale bar=50µm. (C-G) Dendrite arbor parameters in control
396 (+/+, n=10), *ppk-Gal4*-driven Rab11-RNAi (n=10), and *ppk-Gal4*-driven Rab11-RNAi and
397 Spir::GFP (n=12). Asterisks indicate significant changes compared to +/+ controls. (B) Total

398 number of terminal dendrites (ANOVA (F(2,29) = 41.06 p<0.0001). (C) Total length of
399 dendrite arbor (mm) (ANOVA (F(2,29) = 163.6, p<0.0001). (D) Dendritic field (mm^2)
400 (ANOVA (F(2, 29) = 34.00, p<0.0001). (E) Sholl critical value (ANOVA (F(2, 29) = 79.84,
401 p<0.0001) (F) Sholl profiles. (G) Filmstrip (Supplemental Video 7) of control (+/+) L2 larva,
402 where Rab11::GFP (arrows) was observed at the initiation site of a new dendrite branch. Scale
403 bar = 2µm. (H) Distance of the closest Rab11::GFP puncta from the site of branch initiation
404 (n=48) in control (+/+) L2 larvae. (I, J) Dendrite parameters from time lapse movies of control
405 (+mCD8::GFP, n=72 new branches, 10 movies), *ppk-Gal4*-driven Rab11-RNAi (n=6 new
406 branches, 11 movies) or *ppk-Gal4*-driven Rab11-RNAi and Spir::GFP (n=18 new branches, 9
407 movies). (I) Terminal branches/μm^2 in first movie frame (ANOVA F(2,27)=12.41, p=0.0002).
408 (J) Number of new branches/μm^2/min in each movie (ANOVA F(2,27) =14.29, p<0.0001).
409
410 **Figure 6. Spire interacts with Rab11 in c4da neurons.** (A) *ppk-GAL4*-driven Spir::GFP
411 (green) and Rab11::mCherry (magenta, in overlay at right). The cell body of a c4da neuron is
412 indicated (white arrowheads). Co-localization of Spir::GFP and Rab11::mCherry is observed
413 at branch points (e.g., orange arrowhead) and dendrite shafts (e.g., blue arrowhead). Scale
414 bar=50µm. (B) Spir::tdTom co-immunopreciptates with either Capu::GFP (left) or
415 Rab11::GFP (right) from adult head lysates. (C) Dendrite arbors of c4da neurons in $spir^{2F}$/+
416 heterozygotes (left), $Rab11^{Bi93}$ heterozygotes (middle), and trans-heterozygotes for both
417 (right). (D-F) Dendrite arbor parameters in *spir* heterozygotes ($spir^{2F}$/+, n=15), *Rab11*
418 heterozygotes ($Rab11^{Bi93}$/+, n=17), and trans-heterozygotes ($spir^{2F}$/+; $Rab11^{Bi93}$/+, n=15).
419 Asterisks indicate significant changes compared to $spir^{2F}$/+ heterozygous controls (*P<0.05).
420 (D) Total number of terminal dendrites (ANOVA (F(2, 44) = 4.745 p = 0.0136). (E) Total
421 length of dendrite arbor (mm) (ANOVA (F(2, 44) = 5.443, p =0.0077). (F) Dendritic field
422 (mm^2) (ANOVA (F2, 44) = 0.8512, p=0.4338).

423

424 **Materials and Methods**

425 ***Drosophila* stocks and genetics:** Fly stocks were obtained from the Bloomington
426 Drosophila Stock Centre (*spir*^{1}, *spir*^{2F}, *spir*^{DfExel6046} (referred to as *spir*^{Df}), Mi05646, Mi05737,
427 *UAS-capu::GFP*, *Rab11*^{Bi93}, *w*^{1118}, *UAS-mCD8::GFP*, *UAS-Rab11::GFP*, *UAS-Rab6::GFP*,
428 *UAS-Rab11-dsRNA* (referred to as *UAS-Rab11-RNAi*), *UAS-LifeAct-GFP*. *ppk-GAL4* and
429 *ppkCD4::tdTom* and *ppkCD4::GFP* were gifts from Dr. Yuh-Nung Jan. *UAS-Rab11::mCherry*
430 was a gift from Dr. Gregory Emery. *nSyb-GAL4* line was created by Dr Julie Simpson, for
431 which we used 2nd chromosome insertions generated by Dr Stefan Thor. To create the lines
432 *UAS-spir::GFP*, *UAS-spir::tdTom*, *UAS-spir*^{Y232K}*::GFP*, *UAS-spir*^{ABCD}*::GFP*, *UAS-*
433 *spir*$^{\Delta SB}$*::GFP*, *UAS-spir*^{C5,6S}*::GFP*, DNA constructs encoding full-length Spir or each of the 4
434 mutated versions [24,28,40] were designed to add C-terminal GFP or tdTomato (tdTom)
435 fluorophores. These constructs were subcloned into the vector pMUH, then microinjected by
436 standard procedures (Bestgene, Inc) to target the VK00027 landing site in the *Drosophila*
437 genome with φc31-mediated integration[57]. *spir*^{GAL4} was generated by inserting a so-called
438 Trojan-GAL4 into the *spir* locus[58,59]. pT-GEM(0) a gift from Benjamin White (Addgene
439 plasmid # 62891) was microinjected (Bestgene, Inc) into MiMIC line, Mi05646[58,59]. The same
440 plasmid was injected into MiMIC line Mi05737 to generate *capu*^{GAL4}. CRISPR/Cas9-mediated
441 homologous recombination was used to introduce spaghetti-monster GFP-HA (smGFP-HA)[60]
442 into the *spir* locus. To generate Spir-smGFP-HA flies, we used an approach combining dual
443 guide RNA (gRNA) sequences[61] and short homology arms[62]. The CRISPR Optimal Target
444 finder (http://targetfinder.flycrispr.neuro.brown.edu/index.php) was used to select gRNA
445 sequences for the C-terminus of Spir (5'-GTCGGCCCTGGATCTGACGCCCGTC-3') and
446 just after the 3'UTR (5'-GTCGGCAAACTAAAGAACAAGATTC-3'), and these
447 oligonucleotides were cloned into pCFD3-dU6:3gRNA (Addgene plasmid #49410)[63].

448 Homology sequences on 200 nucleotides (PAM removed) were cloned into a self-linearizable
449 Puc573 vector for homologous recombination[62]. The repair template included smGFP-HA, the
450 endogenous 3'UTR of Spir, and the fluorescent eye reporter 3xP3-dsRed, all flanked by two
451 PiggyBac recombinase sites. Plasmids expressing the gRNAs (100ng/µL) and donor template
452 (250ng/µL) were mixed and micro-injected into nos-Cas95 embryos[64] (BDSC 78782). Progeny
453 were screened via fluorescence for the 3xP3-dsRed reporter, and fly stocks were established.
454 All injections and initial screening were completed by BestGene (Chino Hills, CA). Proper
455 insertion of smGFP was confirmed via genomic PCR (primers 5'-
456 GGGGATTCAACCTGTTCTCCT-3' and 5'-TGTGCAAGTGCGTTCTGAAG-3'), and
457 expression confirmed by western blot.

458 **Antibodies:** To produce anti-Spir antisera, DNA encoding Spir amino acids 565-692
459 were cloned into pGEX-6P-1 to produce an IPTG-inducible C-terminal GST fusion proteins in
460 BL21 cells. The purified GST fusion protein was injected into two rabbits and the serum was
461 extracted according to approved protocols at the Comparative Medicine and Animal
462 Resources Centre (McGill University) and standards established by the Canadian Council on
463 Animal Care. Crude serum (500 µl) was then pre-absorbed by overnight incubation with 500
464 µl L3 larvae ($spir^{1}/spir^{Df}$) that had been fixed previously in 4% PFA. Other primary antibodies
465 for IHC were Alexa-647-conjugated goat anti-HRP (1:800, Jackson ImmunoResearch
466 #123605021) and rabbit anti-HA (1:300, Cell Signaling Technology #3724), while the
467 secondary antibody for anti-Spir was Alexa-647-conjugated goat anti-rabbit (1:1000,
468 Invitrogen, #A21244), and for anti-HA IHC it was Alexa-405-conjugated goat anti-rabbit
469 (1:1000, Invitrogen, #A48254). For western blotting, membranes were incubated with mouse
470 anti-GFP (Clontech #632380), rabbit anti-DsRed (Takara #632496), mouse anti-Actin (Sigma
471 #A4700) or rabbit anti-Spire (directed at amino acids 565-692). For detection, HRP-conjugated

472 secondary antibodies (anti-mouse and anti-rabbit (both 1:3000, BioRad) were used and
473 revealed with chemiluminescence (Amersham ECL Western Blotting Detection Reagents).

474 **Immunohistochemistry (IHC):** L3 larvae of either sex were dissected in Sorensen
475 phosphate buffer (pH 7.4) and fixed in 4% paraformaldehyde (in Sorensen's buffer) for 10
476 minutes (min) at room temperature. Washes (3X over 20 min) were done with Sorensen's
477 buffer containing 0.2% Triton-X-100 (Sigma). Specimens were then blocked with Sorensen's
478 buffer containing 5% normal goat serum (NGS), incubated at 4°C with primary antibodies
479 overnight, washed as above, then incubated with secondary antibodies for 2 hours at room
480 temperature. Anti-Spir antiserum for immunohistochemistry was directed at amino acids 1-91.
481 Primary and secondary antibodies were diluted in Sorensen's buffer containing 5% NGS. After
482 a final wash as above, specimens were then mounted with SlowFade Diamond Antifade
483 Mountant (Invitrogen) for imaging.

484 **Co-immunoprecipitation (co-IP) and western blotting:** Lysates for co-IPs and
485 western blots were made from adult heads aged 1-5 days after eclosion. For western blots,
486 heads were mechanically crushed using a motorized pestle directly in 2X Laemmli buffer. For
487 co-IPs, 100 heads were cut and collected on dry ice, then mechanically crushed using a
488 motorized pestle in 100ul of lysis buffer containing 50mM Tris pH, 150mM KCl, 1mM MgCl2,
489 1mM EGTA, Roche protease inhibitor cocktail and 10% glycerol. Lysates were treated with
490 10% deoxycholic acid and 10% Triton X-100, then incubated overnight on a Nutator with anti-
491 GFP bound agarose beads (Chromotek GFP-Trap® #gta). Lysates and beads were separated in
492 a centrifuge, washed with a glycerol free buffer, and the complexes on the beads were
493 dissociated directly in Laemmli buffer, then separated using standard SDS-PAGE and wet-
494 transfer procedures.

495 **Imaging:** All imaging and quantification was of ddaC, the dorsal-most c4da neuron,
496 in abdominal segments of the larval body wall. For static images, L3 larvae were dissected and

497 prepared for IHC, or they were squished directly on the slide in 100% glycerol and prepared
498 for imaging of native fluorescence (GFP, tdTom, mCherry, mRFP) within 10 minutes. Static
499 images were taken with an Olympus Fluoview FV-1000/BX63 confocal microscope using
500 either a 20X or 60X oil-immersion objective lens. All time-lapse imaging was done on L2
501 larvae, where eggs were initially collected for 4h on agar plates containing grape juice and
502 yeast. After 24h, hatched larvae of selected genotypes were transferred on a fresh fly food plate
503 to start timing. L2 larvae (65h ± 4h AEL) were mounted in a drop of halocarbon oil in a
504 polydimethylsiloxane (PDMS) microfluid device, and then imaged by live confocal
505 microscopy (Zeiss, Spinning Disk, Inverted Axio Observer Z1) with 63x objective lens, at
506 room temperature with Immersol W (Zeiss) between lens and coverslip. Using Zen software
507 (Zeiss), live imaging of fluorescent proteins GFP and tdTomato was performed for 5 min with
508 5s interval on average. If GFP only, then the interval was 2s on average. Only movies obtained
509 from larvae that were still alive and active after imaging were used for analysis. Each movie
510 was then registered on ImageJ using StackReg plugin before analysis[65].

511 **Quantification of Lifeact::GFP and Spir::GFP localization:** New branches
512 appearing in each movie were identified, and initiation sites were classified as having *de novo*
513 actin polymer if a punctum of LifeAct::GFP intensity appeared at the site and grew in intensity
514 until protrusion of the new branch. Initiation sites had "pre-formed" actin if motile blobs of
515 LifeAct::GFP were observed to arrive prior to branch outgrowth (motile). Instances where a
516 new branch grew from a site where a LifeAct::GFP punctum existed in the first frame of the
517 movie were disregarded because the movie did not capture the origin of the actin punctum.
518 Consistent with a previous report[16], we observed only a single rare instance where a filopodium
519 grew from an initiation site where LifeAct::GFP was not detected. Overall LifeAct::GFP
520 expression in *spir* mutants appeared lower than in controls, consistent with our previous report

521 for Spir knockdown with RNAi[23], but it was certainly sufficient to monitor actin polymer at
522 sites of branch initiation.

523 To measure the association of Spir::GFP labeled punctae to either a dendrite shaft,
524 branch point, or tip, a custom routine was developed to extract this information from images
525 acquired with a 20X objective (2 to 4 images stitched together where necessary using the
526 Pairwise Stitching plugin[66]. From maximum intensity projections (MIP) of 10 c4da neurons
527 (ddaC) labeled for the dendrite marker CD4-tdTom, signal from beyond the cell of interest was
528 cleared manually, the background was subtracted, and a MIP mask created. This mask was then
529 applied to the SpirFL::GFP channel. Pixels outside the mask were cleared. The MIP mask was
530 skeletonized using Fiji's skeletonization plugin[67] to obtain the location of shafts, branch points,
531 and tips. A script from the Neuroantomy update site was then used to determine which
532 Spir::GFP punctae were associated with such skeleton features. When a Spir::GFP punctum
533 was 3 µm or less (snap-to distance) from either a branch point or tip it was assigned to each,
534 respectively. This snap-to distance was selected because from a representative Spir:GFP image,
535 80% of the punctae had a diameter of 3 µm or less. Additionally, no branch points or tips were
536 3 µm or less apart from one another. The number of punctae at branch points and tips was then
537 divided by the total number of branch points and tips, respectively, to obtain the percent of
538 branch points and tips that were occupied by Spir::GFP.

539 **Dendrite morphometry**: For morphometry of c4da neurons (ddaC) at L3, images were
540 acquired at 20X, with 1 image field usually sufficient to capture the entire dendritic field of a
541 neuron. However, in some cases 2 images were stitched together using the Fiji plugin Pairwise
542 Stitching to generate an image of the entire neuron[66]. Maximum intensity projections of
543 confocal z-series image stacks were segmented as described previously[23]. Various Fiji plugins
544 were used to determine branching characteristics of neurons; Sholl Analysis to generate Sholl
545 profiles and extract Sholl related parameters[68], Strahler Analysis to assess the number of

546 terminal dendrites[68,69], and Analyze Skeleton for total arbor length. Dendritic field was
547 determined by fitting a polygon around the segmented neuron on Fiji, and measuring the area
548 inside the shape[70]. For morphometry of ddaC neurons at L2 in time-lapse movies, the number
549 of terminal dendrites/μm^2 was calculated in the first frame of each movie. For the duration of
550 each movie, the number of new branches/μm^2/minute was calculated.

551 **Measuring dendrite dynamics:** Pre-existing dendrites at the beginning of live imaging
552 movies were analyzed for the dynamics of their terminal branches using MTrackJ[71]. Terminal
553 branch length was compared by an observer every frame of each movie. Dendrites that
554 extended, retracted, or did both, or remained static were recorded, and these numbers were
555 expressed as the percentage of the total number of pre-existing dendrites at the beginning of
556 each movie. Newly formed dendrites were tracked similarly, and their protrusive outgrowth
557 was measured, where mean speed was the average of the speeds of growth for each frame
558 (including extensions and pauses) until the branch stopped growing altogether, or retracted, or
559 the movie ended. The proportion of time the branch spent paused during this period of saltatory
560 outgrowth was calculated, as was the maximum length of its protrusion.

561 **Graphs and Statistics:** Bar graphs and statistics were done using GraphPad Prism v9,
562 and displayed data is expressed as mean ± standard error (SEM). Asterisks indicate the
563 significance of P-values compared to the indicated control group (*P<0.05, **P<0.01,
564 ***P<0.001, ****P<0.0001). For comparisons of more than two conditions, data were tested
565 for normal distribution using D'Agostino & Pearson test and analysed for statistical
566 significance using one-way ANOVA (multiple groups) and Dunnett's post-hoc tests were
567 performed. For the repeated measures of western blots, Friedman test was applied then Dunn's
568 post-hoc tests. To compare two conditions, Student's t-test (unpaired, two-tailed) was used.

569

570 **Supplemental Information**

571 **Supplemental Figure S1: Spir expression and motility in dendrites** (related to Figure 2).
572 (A, B) IHC co-labeling for endogenous Spir and horseradish peroxidase (HRP) in the body
573 wall of L3 larvae, showing Spir expression in a *spir*^{1}/+ heterozygote (A) but not in a *spir*$^{1/Df}$
574 hemizygous mutant (B). (C, D) IHC to detect HA-tagged Spir in a Spir-smGFP-HA larva,
575 focusing on cell body of a c4da neuron (C), and distal dendrite arbors (D). (E) ppk-Gal4 driven
576 Spir::GFP expression is detected with native GFP fluorescence in a c4da neuron labelled with
577 tdTom in an L3 larva. In A-E, labelled c4da neuron cell bodies are marked (white arrowheads),
578 as are puncta in dendrite shafts (blue arrowheads in D), branch points (orange arrowhead in E),
579 and tips (yellow arrowhead E). Scale bars in A-D = 25um, E = 10 um. (F) Locations of
580 Spir::GFP puncta observed in static images of c4da dendrite arbors at L3 (n=10 neurons). (G)
581 Anti-Spir western blot of lysates from dissected adult brains, comparing controls with *spir*$^{1/Df}$
582 mutants and with flies overexpressing Spir::GFP in all neurons with nSyb-Gal4. Expected mass
583 of Spir::GFP is 142kDa, while that of Spir is 115kDa. The increased presence of Spir (115
584 kDa) upon overexpression of Spir::GFP likely arises from proteolytic cleavage of the GFP tag.
585 (H) Greyscale filmstrip (Supplemental Video 4) from a c4da neuron of an L2 larva, where the
586 black arrowhead indicates progressive movement of a Spir::GFP-labelled punctum within a
587 dendrite shaft. Scale bar: 5µm. Motile Spir::GFP puncta moved in both anterograde (64%) and
588 retrograde (36%) directions from the cell soma, and sometimes were observed to switch from
589 one to the other. Some puncta appeared to pass one another, while others merged. Motile
590 Spir::GFP particles were found to travel 0.6 um/s on average, and achieved a maximal speed
591 of 1.1 um/s.
592
593 **Supplemental Figure S2: Quantification of dynamics of newly formed and pre-existing**
594 **terminal branches** (related to Figure 2). (A-B) Dendrite parameters from time-lapse movies
595 of c4da neurons (labeled with ppkCD4::tdTom) in L2 larvae expressing LifeAct::GFP driven

596 by *ppk-GAL4.* Graphs show mean ± SEM, comparing controls (+/+, n=11 movies) with *spir*
597 heterozygotes ($spir^{2F}$/+, n=8) and *spir* mutants ($spir^{2F}/spir^{Df}$, n=11). Asterisks indicate
598 significant changes compared to +/+ controls. (A) Number of terminal branches per μm^2 of
599 area in first frame of each movie (ANOVA (F(2, 27) = 4.079, p = 0.0283). (B) Number of new
600 branches/μm^2/min in each movie (ANOVA (F(2, 27) = 3.265, p = 0.0537). (C-E) Protrusive
601 growth characteristics of nascent branches in controls (+/+, n=14 movies) and *spir* mutants
602 ($spir^{2F}/spir^{Df}$, n=7) in L2 larvae expressing LifeAct::GFP driven by *ppk-GAL4*, including mean
603 speed (C, t-test (t(21) = 1.757, p = 0.0951), time paused (D, t-test(t(21) = 0,7025, p = 0.4909),
604 and maximum protrusion length (E, t-test (t(21) = 1.516, p = 0.1459). Graphs show scatter plot
605 for each branch, with mean ± SEM indicated (ns, not significant). (F-I) For branches that were
606 already present in the first frame of each movie, quantification of percentage of pre-existing
607 branches that extended (F, ANOVA (F (2, 62) = 2.482, p=0.0919), retracted (G, ANOVA (F
608 (2, 62) = 0.6473, p=0.5269), extended and retracted in the same movie (H, ANOVA (F (2, 62)
609 = 4.058, p=0.0221) or remained static (I, ANOVA (F (2, 62) = 4.389, p=0.0165). Results in F-
610 I are combined for neurons that expressed LifeAct-GFP and those that did not, since LifeAct-
611 GFP does not affect the number or dynamics of pre-existing branches. Graphs show mean ±
612 SEM, comparing controls (+/+, n=21 movies) with *spir* heterozygotes ($spir^{2F}$/+, n=18) and *spir*
613 mutants ($spir^{2F}/spir^{Df}$, n=26).
614
615 **Supplemental Figure S3: Dendrite parameters for c4da neurons in L3 larvae** (related to
616 Figure 3). (A-D) This is the same dataset shown in Fig. 3, except it was adjusted to control for
617 dendritic field size by removing from the analysis four $spir^{2F/Df}$ c4da neurons with unusually
618 small arbors (n=11). Asterisks indicate significant changes compared to $spir^{2F}$/+ heterozygous
619 controls. (A) Dendritic field per neuron (mm^2) (ANOVA (F(4, 66) = 1.912, p = 0.1189. (B)
620 Total number of terminal dendrites per neuron (ANOVA (F(4, 66) = 9.328, p < 0.0001). (C)

621 Total length of dendrite arbor per neuron (mm) (ANOVA ($F(4,66) = 12.03$, $p < 0.0001$). (D)
622 Sholl critical value (ANOVA ($F(4, 66) = 6.914$, $p = 0.0001$).
623
624 **Supplemental Figure S4: Function, expression, and distribution of Spir::GFP bearing**
625 **domain-specific mutations** (related to Figure 4). (A) Sholl profiles for entire c4da neurons
626 labelled with ppk-CD4::tdTom. (B) Anti-GFP western blot from adult heads of animals
627 overexpressing in all neurons either intact Spir::GFP or Spir::GFP bearing domain-specific
628 mutations. One of three replicate blots, this blot is distinct from the one shown in Fig. 4C and
629 is shown in its entirety. The expected molecular weight of Spir::GFP is 142 kDa, and that of
630 GFP is 27 kDa, and so proteolytic cleavage of GFP is not apparent for most constructs. (C)
631 *ppk-GAL4* drives the expression of $Spir^{Y232K}$::GFP or $Spir^{ABCD}$::GFP or $Spir^{C5,6S}$::GFP in a *spir*
632 mutant background. Punctate distribution of Spir::GFP is maintained for each of these
633 mutations. White boxes in left panels indicate areas magnified in panels to their right. Scale
634 bar=50μm.
635
636 **Supplemental Figure S5: Effects of overexpression of Spir domain-specific mutations on**
637 **c4da dendrite arborization in wild-type (+/+) animals** (related to Fig. 4)**.** (A-E) Dendrite
638 parameters (mean ± SEM) in wild-type L3 larvae (+/+) expressing Spir::GFP ("+ Spir"), or
639 Spir:GFP with domain-specific mutations (n=8-10 for each genotype). Asterisks indicate
640 significant changes compared to + Spir controls (white bar). All animals in this study bore ppk-
641 Gal4 and ppk-CD4::tdTom transgenes. (A) Total number of terminal dendrites per neuron
642 (ANOVA $F(4, 40) = 3.141$, $p = 0.0245$). (B) Total length of dendrite arbor per neuron (mm)
643 (ANOVA $F(4, 40) = 1.783$, $p = 0.1513$). (C) Dendritic field per neuron (mm^2) (ANOVA $F(4,$
644 $40) = 1.843$, $p = 0.1397$). (D) Sholl profiles. (E) Sholl critical value (ANOVA $F(4, 40) = 1.716$,
645 $p = 0.1655$).

646

647 **Supplemental Figure S6: Effects of Rab11 on dendrite dynamics at L2 and dendrite**
648 **arborization at L3** (related to Figure 5). (A-D) Dendrite parameters from time-lapse movies
649 of c4da neurons (labeled with ppkCD4::tdTom) in L2 larvae. Graphs show mean ± SEM,
650 comparing controls expressing mCD8::GFP (n=10 movies) with Rab11-RNAi driven by *ppk-*
651 *GAL4* (n=11) and Rab11::GFP driven by *ppk-GAL4* (n=10). Asterisks indicate significant
652 changes compared to controls. For branches that were already present in the first frame of each
653 movie, quantification of percentage of pre-existing branches that extended (A, ANOVA (F (2,
654 28) = 2.301, p = 0.1188), retracted (B, ANOVA (F (2, 28) = 0.5551, p = 0.5802), extended and
655 retracted in the same movie (C, ANOVA (F (2, 28) = 8.343, p = 0.0014) or remained static
656 (D, ANOVA (F (2, 28) = 16.50, p<0.0001). (E-H) Dendrite parameters (mean ± SEM) in
657 control L3 larvae (+/+) and ppk-GAL4-driven Rab11::GFP (n=10 for each genotype). Asterisks
658 indicate significant changes compared to controls. (G) Total number of terminal dendrites per
659 neuron (t-test, t(18) = 0.5270 , p = 0.6046). (H) Total length of dendrite arbor per neuron
660 (mm) (t-test, t(18) = 0.0571 , p = 0.9550). (I) Dendritic field per neuron (mm^2) (t-test, t(18) =
661 3,551 , p = 0.0023). (I) Sholl critical value (t-test, t(18) = 0.1905 , p = 0.8510). (J) Sholl profiles.
662

663 **Supplemental Figure S7: Expression, and distribution of Spir::GFP upon Rab11**
664 **knockdown in c4da neurons** (related to Figure 5). (A, B) Distribution of Spir::GFP in c4da
665 neurons of L3 larvae in controls (+/+, A) and upon Rab11 RNAi knockdown in c4da neurons
666 with *ppk-Gal4* (B). White boxes in left panels indicate areas magnified in panels to their right.
667 Upon knockdown of Rab11 in c4da neurons, Spir::GFP retained punctate distribution within
668 dendrite arbors. Scale bars=50µm. (C) Filmstrip (Supplemental Video 8) of Rab11 knockdown
669 L2 larva, where Spir::GFP (arrows) was observed at the initiation site of a new dendrite branch.

670 (D) In Rab11 knockdown c4da neurons, the distance of the closest Spir::GFP puncta from the
671 site of branch initiation (n=18).
672
673 **Supplemental Video 1 – corresponding to Fig. 1C.** 1 frame/7.2s.
674 **Supplemental Video 2 - corresponding to Fig. 1D.** 1 frame/4.4s.
675 **Supplemental Video 3 - corresponding to Fig. 1E.** 1 frame/6.5s.
676 **Supplemental Video 4 - corresponding to Supplemental Fig. S1H.** 1 frame/~2s.
677 **Supplemental Video 5 - corresponding to Fig. 2A.** 1 frame/~4s.
678 **Supplemental Video 6 - corresponding to Fig. 2B.** 1 frame/~7s.
679 **Supplemental Video 7 - corresponding to Fig. 5G** 1 frame/~6s.
680 **Supplemental Video 8 - corresponding to Supplemental Fig. S7C.** 1 frame/~7s.
681
682
683 **References**

684 1. Grueber, W.B., Yang, C.H., Ye, B., and Jan, Y.N. (2005). The development of neuronal
685 morphology in insects. Curr Biol *15*, R730-738.
686 2. London, M., and Hausser, M. (2005). Dendritic computation. Annual review of
687 neuroscience *28*, 503-532.
688 3. Lefebvre, J.L., Sanes, J.R., and Kay, J.N. (2015). Development of dendritic form and
689 function. Annual review of cell and developmental biology *31*, 741-777.
690 10.1146/annurev-cellbio-100913-013020.
691 4. Luo, L. (2021). Architectures of neuronal circuits. Science *373*, eabg7285.
692 10.1126/science.abg7285.
693 5. Lefebvre, J.L. (2021). Molecular mechanisms that mediate dendrite morphogenesis.
694 Curr Top Dev Biol *142*, 233-282. 10.1016/bs.ctdb.2020.12.008.

695 6. Konietzny, A., Bar, J., and Mikhaylova, M. (2017). Dendritic Actin Cytoskeleton:
696 Structure, Functions, and Regulations. Frontiers in cellular neuroscience *11*, 147.
697 10.3389/fncel.2017.00147.
698 7. Siton-Mendelson, O., and Bernheim-Groswasser, A. (2017). Functional Actin
699 Networks under Construction: The Cooperative Action of Actin Nucleation and
700 Elongation Factors. Trends Biochem Sci *42*, 414-430. 10.1016/j.tibs.2017.03.002.
701 8. Rottner, K., Faix, J., Bogdan, S., Linder, S., and Kerkhoff, E. (2017). Actin assembly
702 mechanisms at a glance. J Cell Sci *130*, 3427-3435. 10.1242/jcs.206433.
703 9. Kennedy, M.J., and Hanus, C. (2019). Architecture and Dynamics of the Neuronal
704 Secretory Network. Annual review of cell and developmental biology *35*, 543-566.
705 10.1146/annurev-cellbio-100818-125418.
706 10. Lanoue, V., and Cooper, H.M. (2019). Branching mechanisms shaping dendrite
707 architecture. Dev Biol *451*, 16-24. 10.1016/j.ydbio.2018.12.005.
708 11. Korobova, F., and Svitkina, T. (2010). Molecular architecture of synaptic actin
709 cytoskeleton in hippocampal neurons reveals a mechanism of dendritic spine
710 morphogenesis. Mol Biol Cell *21*, 165-176. E09-07-0596 [pii] 10.1091/mbc.E09-07-
711 0596.
712 12. Sturner, T., Tatarnikova, A., Mueller, J., Schaffran, B., Cuntz, H., Zhang, Y.,
713 Nemethova, M., Bogdan, S., Small, V., and Tavosanis, G. (2019). Transient
714 localization of the Arp2/3 complex initiates neuronal dendrite branching in vivo.
715 Development *146*. 10.1242/dev.171397.
716 13. Zou, W., Dong, X., Broederdorf, T.R., Shen, A., Kramer, D.A., Shi, R., Liang, X.,
717 Miller, D.M., 3rd, Xiang, Y.K., Yasuda, R., et al. (2018). A Dendritic Guidance
718 Receptor Complex Brings Together Distinct Actin Regulators to Drive Efficient F-

719 Actin Assembly and Branching. Developmental cell *45*, 362-375 e363.
720 10.1016/j.devcel.2018.04.008.
721 14. Shi, R., Kramer, D.A., Chen, B., and Shen, K. (2021). A two-step actin polymerization
722 mechanism drives dendrite branching. Neural Dev *16*, 3. 10.1186/s13064-021-00154-
723 0.
724 15. Hou, W., Izadi, M., Nemitz, S., Haag, N., Kessels, M.M., and Qualmann, B. (2015).
725 The Actin Nucleator Cobl Is Controlled by Calcium and Calmodulin. PLoS Biol *13*,
726 e1002233. 10.1371/journal.pbio.1002233.
727 16. Nithianandam, V., and Chien, C.T. (2018). Actin blobs prefigure dendrite branching
728 sites. The Journal of cell biology *217*, 3731-3746. 10.1083/jcb.201711136.
729 17. Sturner, T., Ferreira Castro, A., Philipps, M., Cuntz, H., and Tavosanis, G. (2022). The
730 branching code: A model of actin-driven dendrite arborization. Cell reports *39*, 110746.
731 10.1016/j.celrep.2022.110746.
732 18. Grueber, W.B., Jan, L.Y., and Jan, Y.N. (2002). Tiling of the Drosophila epidermis by
733 multidendritic sensory neurons. Development *129*, 2867-2878.
734 19. Medina, P.M., Swick, L.L., Andersen, R., Blalock, Z., and Brenman, J.E. (2006). A
735 novel forward genetic screen for identifying mutations affecting larval neuronal
736 dendrite development in Drosophila melanogaster. Genetics *172*, 2325-2335.
737 20. Nagel, A.C., Apidianakis, Y., Wech, I., Maier, D., Delidakis, C., and Preiss, A. (2000).
738 Neural hyperplasia induced by RNA interference with m4/malpha gene activity.
739 Mechanisms of development *98*, 19-28.
740 21. Andersen, R., Li, Y., Resseguie, M., and Brenman, J.E. (2005). Calcium/calmodulin-
741 dependent protein kinase II alters structural plasticity and cytoskeletal dynamics in
742 Drosophila. J Neurosci *25*, 8878-8888. 25/39/8878 [pii] 10.1523/JNEUROSCI.2005-
743 05.2005.

744 22. Willig, K.I., Steffens, H., Gregor, C., Herholt, A., Rossner, M.J., and Hell, S.W. (2014).
745 Nanoscopy of filamentous actin in cortical dendrites of a living mouse. Biophys J *106*,
746 L01-03. 10.1016/j.bpj.2013.11.1119.
747 23. Ferreira, T., Ou, Y., Li, S., Giniger, E., and van Meyel, D.J. (2014). Dendrite
748 architecture organized by transcriptional control of the F-actin nucleator Spire.
749 Development *141*, 650-660. 10.1242/dev.099655.
750 24. Quinlan, M.E., Heuser, J.E., Kerkhoff, E., and Mullins, R.D. (2005). Drosophila Spire
751 is an actin nucleation factor. Nature *433*, 382-388. nature03241 [pii]
752 10.1038/nature03241.

753 25. Vizcarra, C.L., Kreutz, B., Rodal, A.A., Toms, A.V., Lu, J., Zheng, W., Quinlan, M.E.,
754 and Eck, M.J. (2011). Structure and function of the interacting domains of Spire and
755 Fmn-family formins. Proc Natl Acad Sci U S A *108*, 11884-11889. 1105703108 [pii]
756 10.1073/pnas.1105703108.

757 26. Manseau, L.J., and Schupbach, T. (1989). cappuccino and spire: two unique maternal-
758 effect loci required for both the anteroposterior and dorsoventral patterns of the
759 Drosophila embryo. Genes & development *3*, 1437-1452.
760 27. Pfender, S., Kuznetsov, V., Pleiser, S., Kerkhoff, E., and Schuh, M. (2011). Spire-type
761 actin nucleators cooperate with Formin-2 to drive asymmetric oocyte division. Curr
762 Biol *21*, 955-960. S0960-9822(11)00468-4 [pii] 10.1016/j.cub.2011.04.029.

763 28. Kerkhoff, E., Simpson, J.C., Leberfinger, C.B., Otto, I.M., Doerks, T., Bork, P., Rapp,
764 U.R., Raabe, T., and Pepperkok, R. (2001). The Spir actin organizers are involved in
765 vesicle transport processes. Curr Biol *11*, 1963-1968. S0960-9822(01)00602-9 [pii].
766 29. Tittel, J., Welz, T., Czogalla, A., Dietrich, S., Samol-Wolf, A., Schulte, M., Schwille,
767 P., Weidemann, T., and Kerkhoff, E. (2015). Membrane targeting of the Spir.formin

768 actin nucleator complex requires a sequential handshake of polar interactions. The
769 Journal of biological chemistry *290*, 6428-6444. 10.1074/jbc.M114.602672.
770 30. Quinlan, M.E., Hilgert, S., Bedrossian, A., Mullins, R.D., and Kerkhoff, E. (2007).
771 Regulatory interactions between two actin nucleators, Spire and Cappuccino. The
772 Journal of cell biology *179*, 117-128. jcb.200706196 [pii] 10.1083/jcb.200706196.
773 31. Yao, L.L., Hou, W.D., Liang, Y., Li, X.D., and Ji, H.H. (2024). Spire2 and Rab11a
774 synergistically activate myosin-5b motor function. Biochem Biophys Res Commun
775 *703*, 149653. 10.1016/j.bbrc.2024.149653.
776 32. Kiral, F.R., Kohrs, F.E., Jin, E.J., and Hiesinger, P.R. (2018). Rab GTPases and
777 Membrane Trafficking in Neurodegeneration. Curr Biol *28*, R471-R486.
778 10.1016/j.cub.2018.02.010.
779 33. Welz, T., and Kerkhoff, E. (2023). The role of SPIRE actin nucleators in cellular
780 transport processes. J Cell Sci *136*. 10.1242/jcs.260743.
781 34. Schuh, M. (2011). An actin-dependent mechanism for long-range vesicle transport.
782 Nature cell biology *13*, 1431-1436. 10.1038/ncb2353 ncb2353 [pii].
783 35. Pylypenko, O., Welz, T., Tittel, J., Kollmar, M., Chardon, F., Malherbe, G., Weiss, S.,
784 Michel, C.I., Samol-Wolf, A., Grasskamp, A.T., et al. (2016). Coordinated recruitment
785 of Spir actin nucleators and myosin V motors to Rab11 vesicle membranes. Elife *5*.
786 10.7554/eLife.17523.
787 36. Kramer, R., Rode, S., and Rumpf, S. (2019). Rab11 is required for neurite pruning and
788 developmental membrane protein degradation in Drosophila sensory neurons. Dev Biol
789 *451*, 68-78. 10.1016/j.ydbio.2019.03.003.
790 37. Lin, T., Kao, H.H., Chou, C.H., Chou, C.Y., Liao, Y.C., and Lee, H.H. (2020). Rab11
791 activation by Ik2 kinase is required for dendrite pruning in Drosophila sensory neurons.
792 PLoS genetics *16*, e1008626. 10.1371/journal.pgen.1008626.

793 38. Mitchell, J.W., Midillioglu, I., Schauer, E., Wang, B., Han, C., and Wildonger, J.
794 (2023). Coordination of Pickpocket ion channel delivery and dendrite growth in
795 Drosophila sensory neurons. PLoS genetics *19*, e1011025.
796 10.1371/journal.pgen.1011025.
797 39. Wellington, A., Emmons, S., James, B., Calley, J., Grover, M., Tolias, P., and Manseau,
798 L. (1999). Spire contains actin binding domains and is related to ascidian posterior end
799 mark-5. Development *126*, 5267-5274.
800 40. Quinlan, M.E. (2013). Direct interaction between two actin nucleators is required in
801 Drosophila oogenesis. Development *140*, 4417-4425. 10.1242/dev.097337.
802 41. Marat, A.L., and Haucke, V. (2016). Phosphatidylinositol 3-phosphates-at the interface
803 between cell signalling and membrane traffic. The EMBO journal *35*, 561-579.
804 10.15252/embj.201593564.
805 42. Sonnichsen, B., De Renzis, S., Nielsen, E., Rietdorf, J., and Zerial, M. (2000). Distinct
806 membrane domains on endosomes in the recycling pathway visualized by multicolor
807 imaging of Rab4, Rab5, and Rab11. The Journal of cell biology *149*, 901-914.
808 43. Gates, M.A., Kannan, R., and Giniger, E. (2011). A genome-wide analysis reveals that
809 the Drosophila transcription factor Lola promotes axon growth in part by suppressing
810 expression of the actin nucleation factor Spire. Neural Dev *6*, 37. 1749-8104-6-37 [pii]
811 10.1186/1749-8104-6-37.
812 44. Lasiecka, Z.M., and Winckler, B. (2011). Mechanisms of polarized membrane
813 trafficking in neurons -- focusing in on endosomes. Mol Cell Neurosci *48*, 278-287.
814 10.1016/j.mcn.2011.06.013.
815 45. Park, M., Penick, E.C., Edwards, J.G., Kauer, J.A., and Ehlers, M.D. (2004). Recycling
816 endosomes supply AMPA receptors for LTP. Science *305*, 1972-1975.
817 10.1126/science.1102026 305/5692/1972 [pii].

818 46. Eva, R., Dassie, E., Caswell, P.T., Dick, G., ffrench-Constant, C., Norman, J.C., and
819 Fawcett, J.W. (2010). Rab11 and its effector Rab coupling protein contribute to the
820 trafficking of beta 1 integrins during axon growth in adult dorsal root ganglion neurons
821 and PC12 cells. J Neurosci *30*, 11654-11669. 10.1523/JNEUROSCI.2425-10.2010.
822 47. Pai, Y.J., and Moore, A.W. (2018). Dendritic actin delivery service. The Journal of cell
823 biology *217*, 3325-3326. 10.1083/jcb.201808095.
824 48. Das, R., Bhattacharjee, S., Letcher, J.M., Harris, J.M., Nanda, S., Foldi, I., Lottes, E.N.,
825 Bobo, H.M., Grantier, B.D., Mihaly, J., et al. (2021). Formin 3 directs dendritic
826 architecture via microtubule regulation and is required for somatosensory nociceptive
827 behavior. Development *148*. 10.1242/dev.187609.
828 49. Manor, U., Bartholomew, S., Golani, G., Christenson, E., Kozlov, M., Higgs, H.,
829 Spudich, J., and Lippincott-Schwartz, J. (2015). A mitochondria-anchored isoform of
830 the actin-nucleating spire protein regulates mitochondrial division. Elife *4*.
831 10.7554/eLife.08828.
832 50. Schumacher, N., Borawski, J.M., Leberfinger, C.B., Gessler, M., and Kerkhoff, E.
833 (2004). Overlapping expression pattern of the actin organizers Spir-1 and formin-2 in
834 the developing mouse nervous system and the adult brain. Gene expression patterns :
835 GEP *4*, 249-255. 10.1016/j.modgep.2003.11.006 S1567133X03002096 [pii].
836 51. Pleiser, S., Rock, R., Wellmann, J., Gessler, M., and Kerkhoff, E. (2010). Expression
837 patterns of the mouse Spir-2 actin nucleator. Gene expression patterns : GEP *10*, 345-
838 350. S1567-133X(10)00080-3 [pii] 10.1016/j.gep.2010.08.001.
839 52. Hao, L., Zhang, H., Peng, X., Yang, Y., Yang, M., Guo, Y., Wang, X., and Jing, W.
840 (2022). Decreased Spire2 Expression is Involved in Epilepsy. Neuroscience *504*, 1-9.
841 10.1016/j.neuroscience.2022.09.008.

842 53. Holubcova, Z., Howard, G., and Schuh, M. (2013). Vesicles modulate an actin network
843 for asymmetric spindle positioning. Nature cell biology *15*, 937-947. 10.1038/ncb2802.
844 54. Alzahofi, N., Welz, T., Robinson, C.L., Page, E.L., Briggs, D.A., Stainthorp, A.K.,
845 Reekes, J., Elbe, D.A., Straub, F., Kallemeijn, W.W., et al. (2020). Rab27a co-ordinates
846 actin-dependent transport by controlling organelle-associated motors and track
847 assembly proteins. Nat Commun *11*, 3495. 10.1038/s41467-020-17212-6.
848 55. Yoong, L.F., Lim, H.K., Tran, H., Lackner, S., Zheng, Z., Hong, P., and Moore, A.W.
849 (2020). Atypical Myosin Tunes Dendrite Arbor Subdivision. Neuron *106*, 452-467
850 e458. 10.1016/j.neuron.2020.02.002.
851 56. Zhang, Y., Sung, H.H., Ziegler, A.B., Wu, Y.C., Viais, R., Sanchez-Huertas, C., Kilo,
852 L., Agrican, F.G., Cheng, Y.J., Mouri, K., et al. (2024). Augmin complex activity fine-
853 tunes dendrite morphology through non-centrosomal microtubule nucleation in vivo. J
854 Cell Sci. 10.1242/jcs.261512.
855 57. Pfeiffer, B.D., Ngo, T.T., Hibbard, K.L., Murphy, C., Jenett, A., Truman, J.W., and
856 Rubin, G.M. (2010). Refinement of tools for targeted gene expression in Drosophila.
857 Genetics *186*, 735-755. 10.1534/genetics.110.119917.
858 58. Diao, F., Ironfield, H., Luan, H., Diao, F., Shropshire, W.C., Ewer, J., Marr, E., Potter,
859 C.J., Landgraf, M., and White, B.H. (2015). Plug-and-play genetic access to drosophila
860 cell types using exchangeable exon cassettes. Cell reports *10*, 1410-1421.
861 10.1016/j.celrep.2015.01.059.
862 59. Venken, K.J., Schulze, K.L., Haelterman, N.A., Pan, H., He, Y., Evans-Holm, M.,
863 Carlson, J.W., Levis, R.W., Spradling, A.C., Hoskins, R.A., and Bellen, H.J. (2011).
864 MiMIC: a highly versatile transposon insertion resource for engineering Drosophila
865 melanogaster genes. Nat Methods *8*, 737-743.

866 60. Viswanathan, S., Williams, M.E., Bloss, E.B., Stasevich, T.J., Speer, C.M., Nern, A.,
867 Pfeiffer, B.D., Hooks, B.M., Li, W.P., English, B.P., et al. (2015). High-performance
868 probes for light and electron microscopy. Nat Methods *12*, 568-576.
869 10.1038/nmeth.3365.
870 61. Bence, M., Jankovics, F., Lukacsovich, T., and Erdelyi, M. (2017). Combining the
871 auxin-inducible degradation system with CRISPR/Cas9-based genome editing for the
872 conditional depletion of endogenous Drosophila melanogaster proteins. The FEBS
873 journal *284*, 1056-1069. 10.1111/febs.14042.
874 62. Kanca, O., Zirin, J., Garcia-Marques, J., Knight, S.M., Yang-Zhou, D., Amador, G.,
875 Chung, H., Zuo, Z., Ma, L., He, Y., et al. (2019). An efficient CRISPR-based strategy
876 to insert small and large fragments of DNA using short homology arms. Elife *8*.
877 10.7554/eLife.51539.
878 63. Port, F., Chen, H.M., Lee, T., and Bullock, S.L. (2014). Optimized CRISPR/Cas tools
879 for efficient germline and somatic genome engineering in Drosophila. Proc Natl Acad
880 Sci U S A *111*, E2967-2976. 10.1073/pnas.1405500111.
881 64. Ren, X., Sun, J., Housden, B.E., Hu, Y., Roesel, C., Lin, S., Liu, L.P., Yang, Z., Mao,
882 D., Sun, L., et al. (2013). Optimized gene editing technology for Drosophila
883 melanogaster using germ line-specific Cas9. Proc Natl Acad Sci U S A *110*, 19012-
884 19017. 10.1073/pnas.1318481110.
885 65. Thevenaz, P., Ruttimann, U.E., and Unser, M. (1998). A pyramid approach to subpixel
886 registration based on intensity. IEEE Trans Image Process *7*, 27-41.
887 10.1109/83.650848.
888 66. Preibisch, S., Saalfeld, S., and Tomancak, P. (2009). Globally optimal stitching of tiled
889 3D microscopic image acquisitions. Bioinformatics *25*, 1463-1465. btp184 [pii]
890 10.1093/bioinformatics/btp184.

891 67. Arganda-Carreras, I., Fernandez-Gonzalez, R., Munoz-Barrutia, A., and Ortiz-De-
892 Solorzano, C. (2010). 3D reconstruction of histological sections: Application to
893 mammary gland tissue. Microsc Res Tech *73*, 1019-1029. 10.1002/jemt.20829.
894 68. Ferreira, T.A., Blackman, A.V., Oyrer, J., Jayabal, S., Chung, A.J., Watt, A.J.,
895 Sjostrom, P.J., and van Meyel, D.J. (2014). Neuronal morphometry directly from
896 bitmap images. Nat Methods *11*, 982-984. 10.1038/nmeth.3125.
897 69. Strahler, A.N. (1957). Quantitative analysis of watershed geomorphology. Transactions
898 of the American Geophysical Union *38*, 913-920.
899 70. Schindelin, J., Arganda-Carreras, I., Frise, E., Kaynig, V., Longair, M., Pietzsch, T.,
900 Preibisch, S., Rueden, C., Saalfeld, S., Schmid, B., et al. (2012). Fiji: an open-source
901 platform for biological-image analysis. Nat Methods *9*, 676-682. 10.1038/nmeth.2019
902 nmeth.2019 [pii].
903 71. Meijering, E., Dzyubachyk, O., and Smal, I. (2012). Methods for cell and particle
904 tracking. Methods Enzymol *504*, 183-200. 10.1016/B978-0-12-391857-4.00009-4.

905

Figure 1

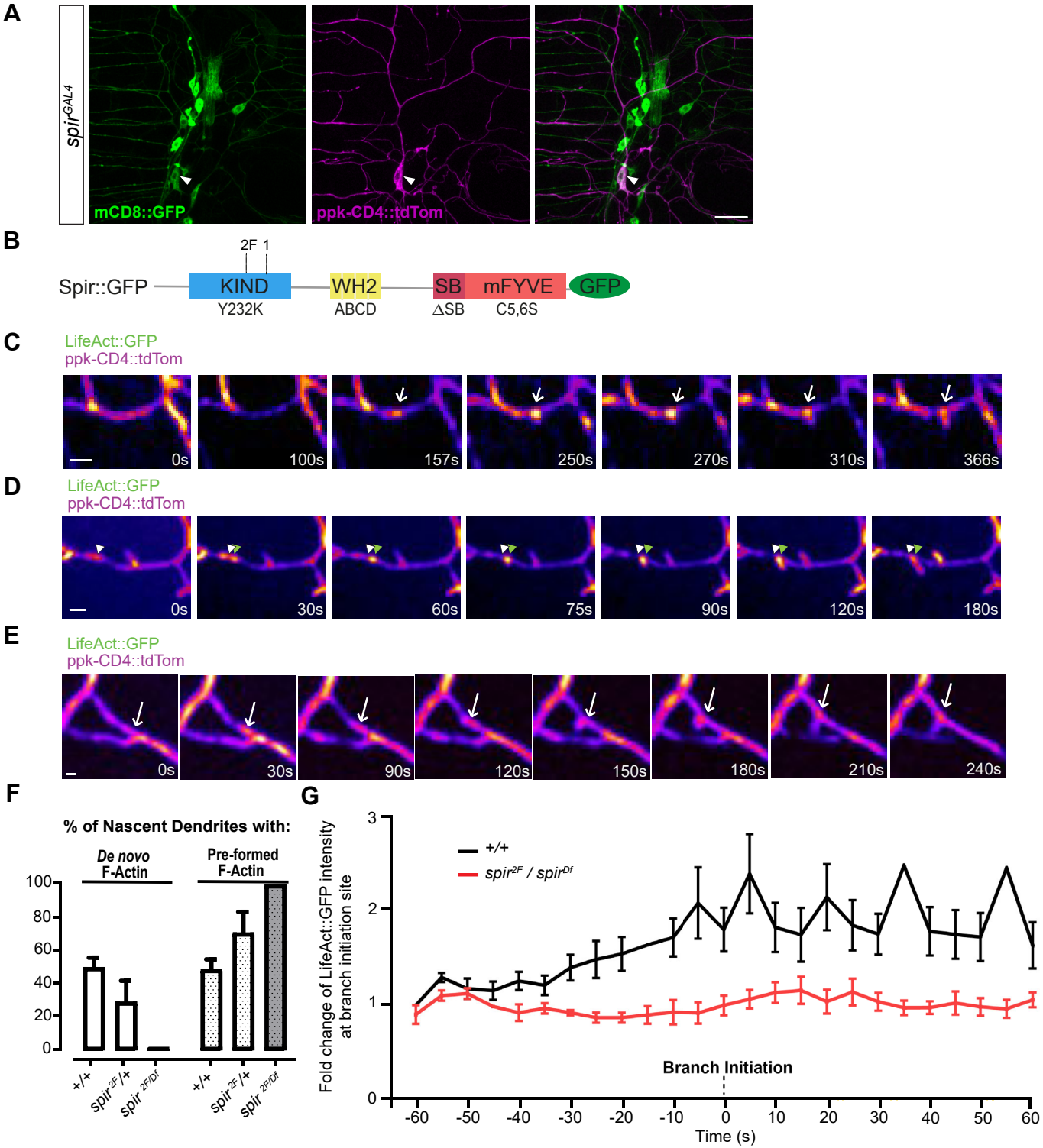
A
spirGAL4
mCD8::GFP
ppk-CD4::tdTom
B
2F 1
Spir::GFP
KIND
Y232K
WH2
ABCD
SB
ΔSB
mFYVE
C5,6S
GFP
C
LifeAct::GFP
ppk-CD4::tdTom
0s
100s
157s
250s
270s
310s
366s
D
LifeAct::GFP
ppk-CD4::tdTom
0s
30s
60s
75s
90s
120s
180s
E
LifeAct::GFP
ppk-CD4::tdTom
0s
30s
90s
120s
150s
180s
210s
240s
F
% of Nascent Dendrites with:
De novo F-Actin
Pre-formed F-Actin
100
80
60
40
20
0
+/+
spir2F/+
spir 2F/Df
+/+
spir2F/+
spir 2F/Df
G
Fold change of LifeAct::GFP intensity at branch initiation site
+/+
spir2F / spirDf
Branch Initiation
Time (s)
-60
-50
-40
-30
-20
-10
0
10
20
30
40
50
60
3
2
1
0

Figure 2

A Spir::GFP
ppk-CD4::tdTom

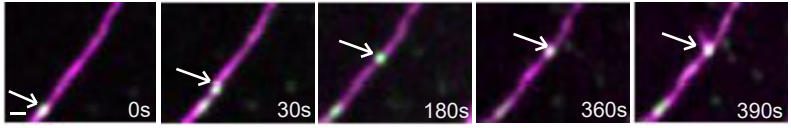

B Spir::GFP
ppk-CD4::tdTom

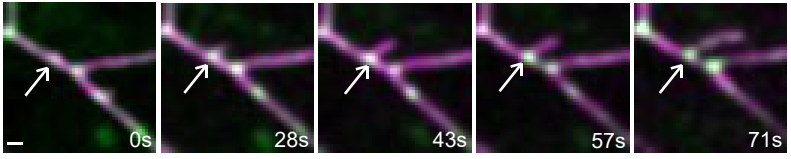

C

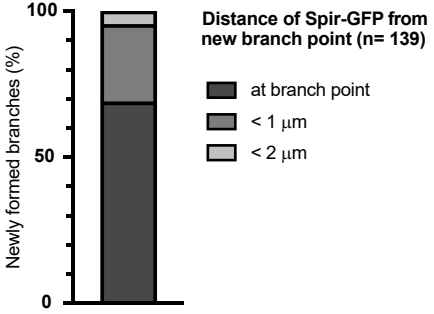

D

Spir::GFP puncta at branch initiation sites in time-lapse movies at L2 (n=61)				
	Occurrence	Time (s) from stationary punctum to branch outgrowth		
		Minimum	Maximum	Mean ±sd
Spir::GFP observed to move to site	30%	4	129	43 ± 41
Spir::GFP stationed at site in first movie frame	70%	8	229	88 ± 67

E

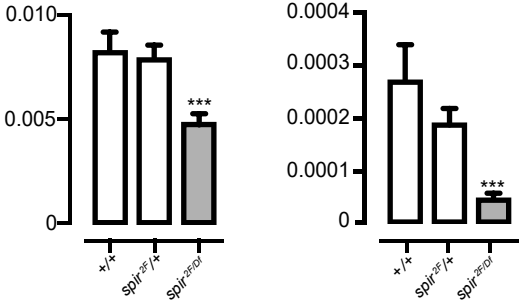

Figure 3

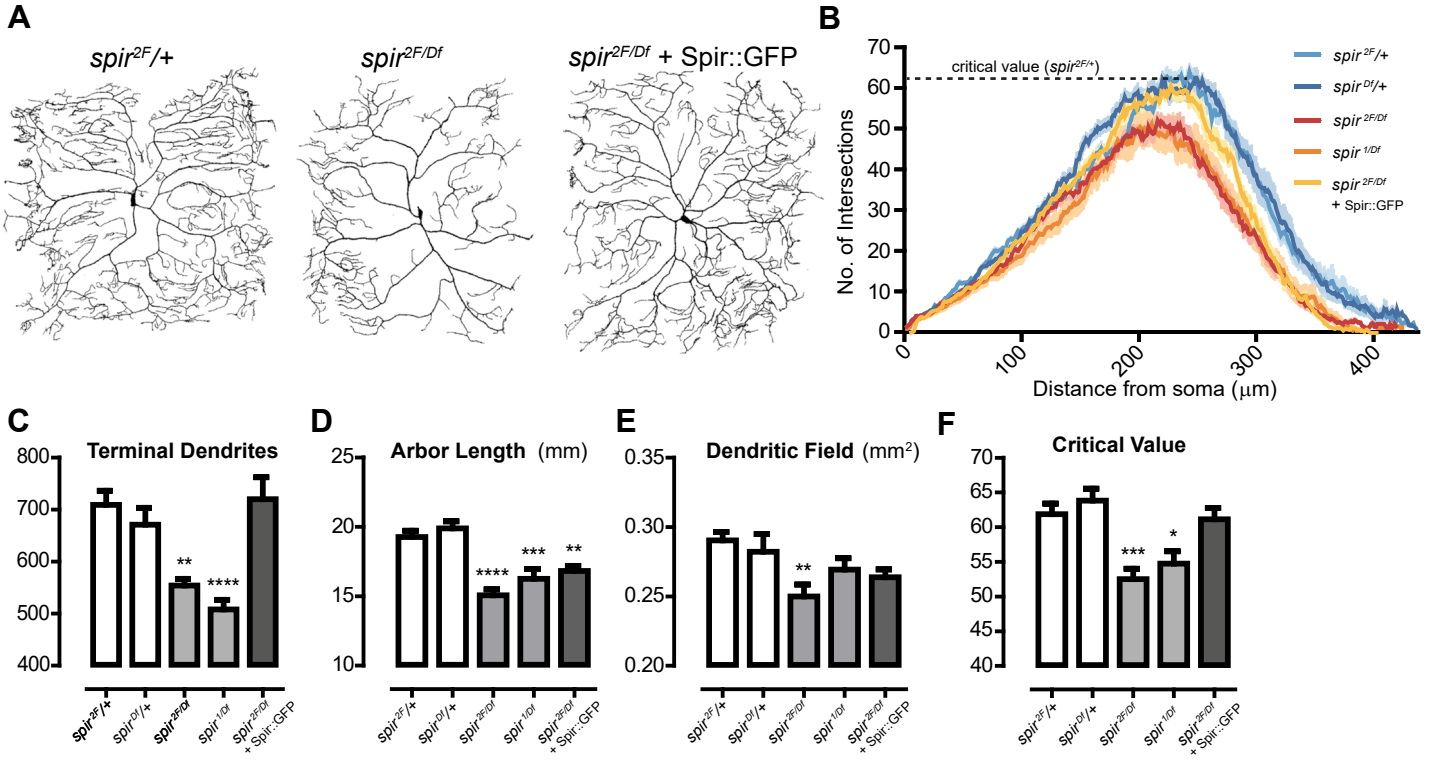
A
spir2F/+
spir2F/Df
spir2F/Df + Spir::GFP
B
critical value (spir2F/+)
No. of Intersections
Distance from soma (μm)
spir 2F/+
spir Df/+
spir 2F/Df
spir 1/Df
spir 2F/Df + Spir::GFP
C
Terminal Dendrites
D
Arbor Length (mm)
E
Dendritic Field (mm2)
F
Critical Value

Figure 4

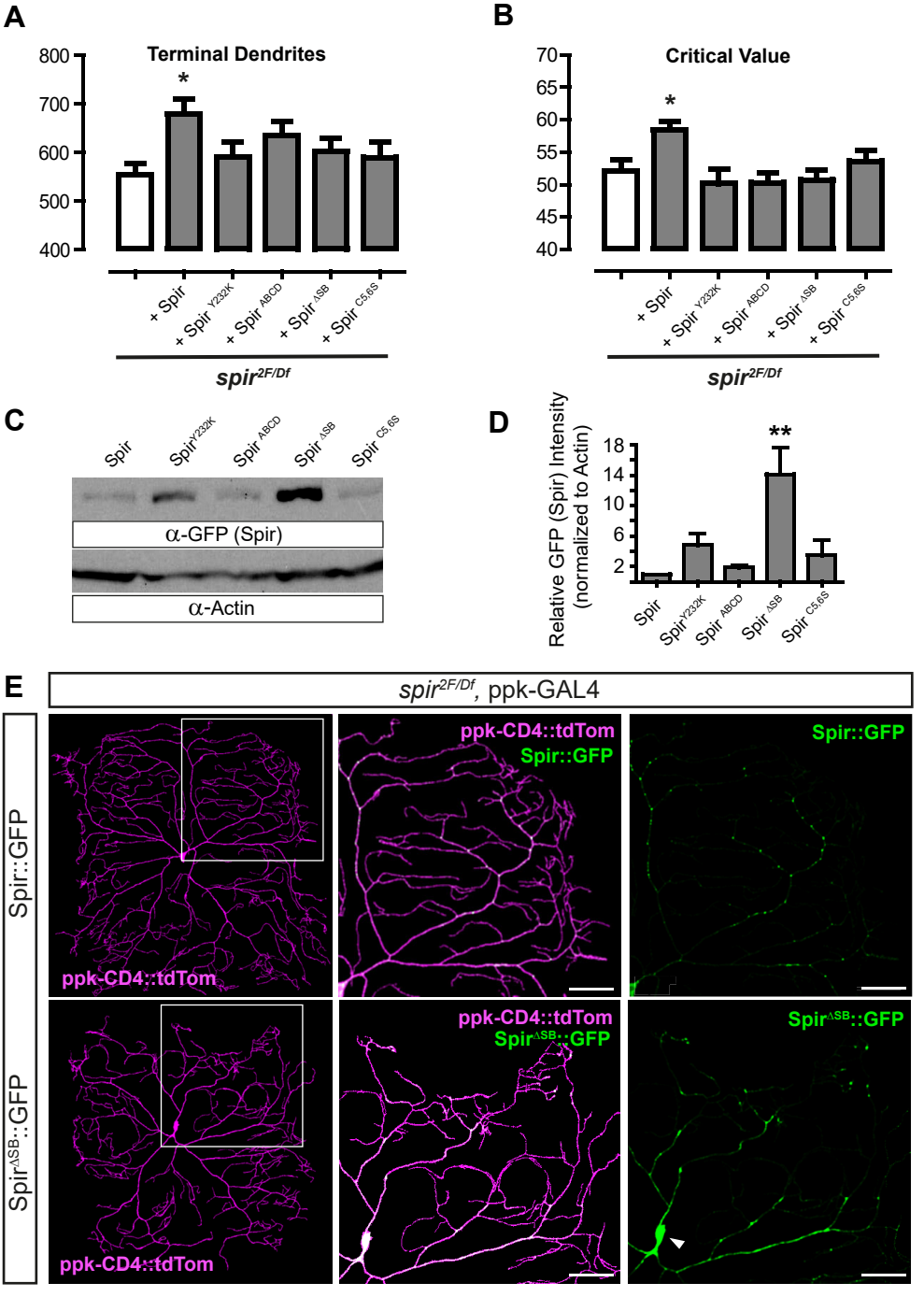
A
Terminal Dendrites
800
700
600
500
400
*
+ Spir
+ Spir Y232K
+ Spir ABCD
+ Spir ΔSB
+ Spir C5,6S
spir2F/Df
B
Critical Value
70
65
60
55
50
45
40
*
+ Spir
+ Spir Y232K
+ Spir ABCD
+ Spir ΔSB
+ Spir C5,6S
spir2F/Df
C
Spir
SpirY232K
Spir ABCD
Spir ΔSB
Spir C5,6S
α-GFP (Spir)
α-Actin
D
Relative GFP (Spir) Intensity (normalized to Actin)
18
14
10
6
2
**
Spir
SpirY232K
Spir ABCD
Spir ΔSB
Spir C5,6S
E
spir2F/Df, ppk-GAL4
Spir::GFP
SpirΔSB::GFP
ppk-CD4::tdTom
ppk-CD4::tdTom
Spir::GFP
Spir::GFP
ppk-CD4::tdTom
ppk-CD4::tdTom
SpirΔSB::GFP
SpirΔSB::GFP

Figure 5

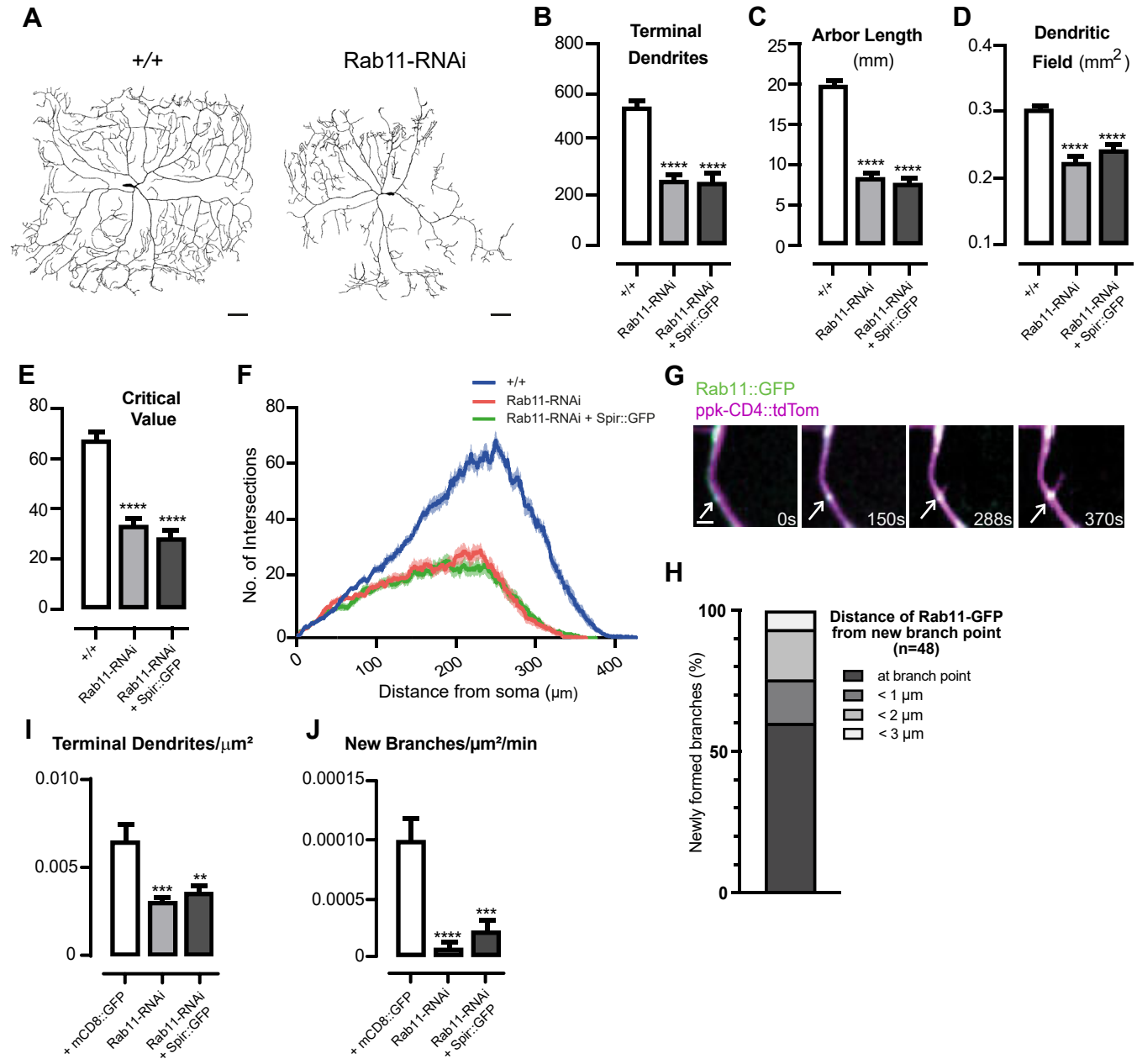
A
+/+
Rab11-RNAi
B
Terminal Dendrites
800
600
400
200
0
****
****
+/+
Rab11-RNAi
Rab11-RNAi + Spir::GFP
C
Arbor Length (mm)
25
20
15
10
5
0
****
****
+/+
Rab11-RNAi
Rab11-RNAi + Spir::GFP
D
Dendritic Field (mm2)
0.4
0.3
0.2
0.1
****
****
+/+
Rab11-RNAi
Rab11-RNAi + Spir::GFP
E
Critical Value
80
60
40
20
0
****
****
+/+
Rab11-RNAi
Rab11-RNAi + Spir::GFP
F
+/+
Rab11-RNAi
Rab11-RNAi + Spir::GFP
No. of Intersections
80
60
40
20
0
0
100
200
300
400
Distance from soma (μm)
G
Rab11::GFP
ppk-CD4::tdTom
0s
150s
288s
370s
H
Distance of Rab11-GFP from new branch point (n=48)
at branch point
< 1 μm
< 2 μm
< 3 μm
Newly formed branches (%)
100
50
0
I
Terminal Dendrites/μm²
0.010
0.005
0
***
**
+ mCD8::GFP
Rab11-RNAi
Rab11-RNAi + Spir::GFP
J
New Branches/μm²/min
0.00015
0.00010
0.0005
0
****
***
+ mCD8::GFP
Rab11-RNAi
Rab11-RNAi + Spir::GFP

Figure 6

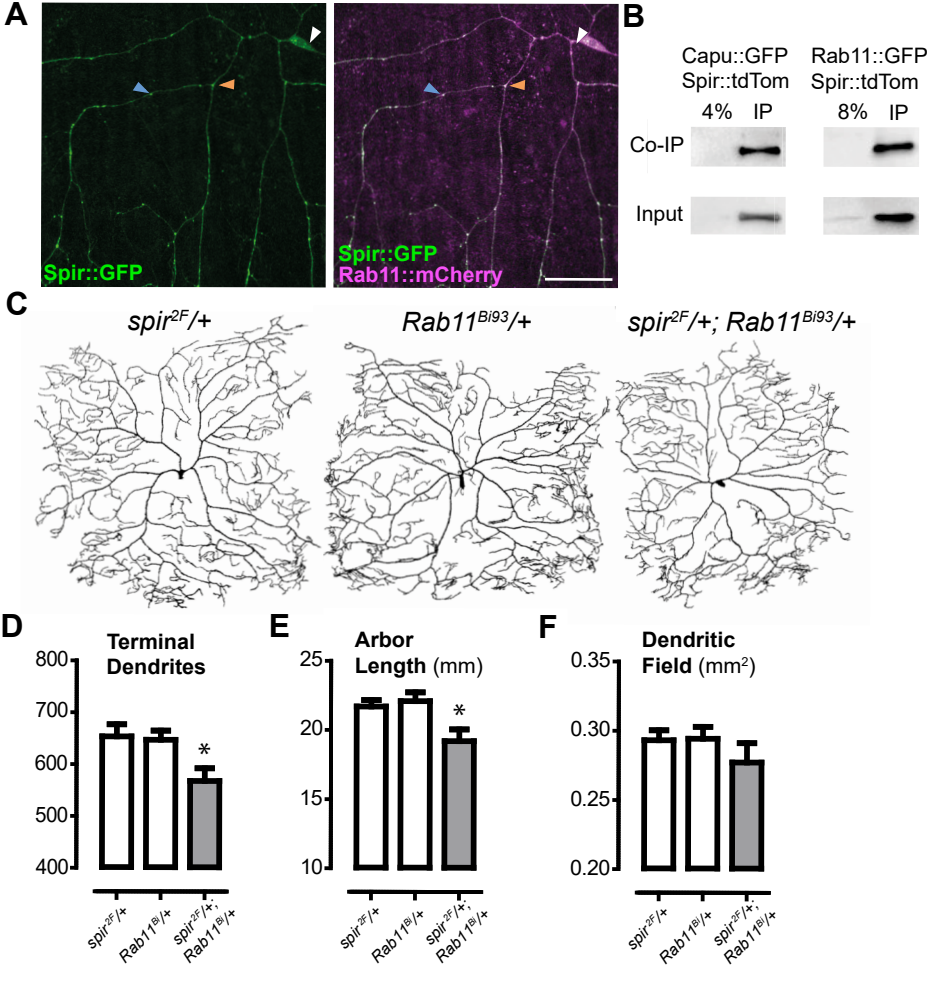
A
Spir::GFP
Spir::GFP
Rab11::mCherry
B
Capu::GFP
Spir::tdTom
Rab11::GFP
Spir::tdTom
4%
IP
8%
IP
Co-IP
Input
C
spir2F/+
Rab11Bi93/+
spir2F/+; Rab11Bi93/+
D
Terminal Dendrites
800
700
600
500
400
*
spir2F/+
Rab11Bi/+
spir2F/+; Rab11Bi/+
E
Arbor Length (mm)
25
20
15
10
*
spir2F/+
Rab11Bi/+
spir2F/+; Rab11Bi/+
F
Dendritic Field (mm2)
0.35
0.30
0.25
0.20
spir2F/+
Rab11Bi/+
spir2F/+; Rab11Bi/+

Figure S1

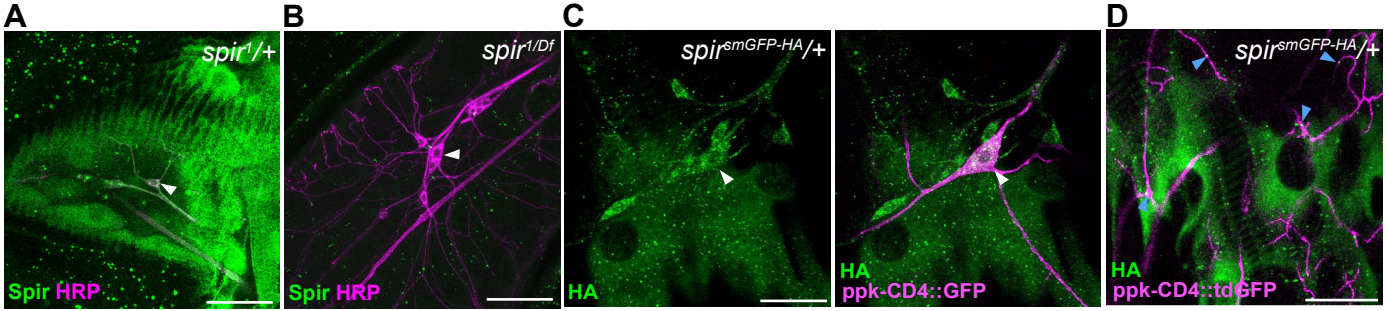

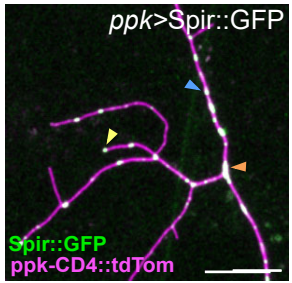

F

Spir::GFP puncta in static images at L3			
	Occurence		
	Shafts	Branch points	Tips
Spir::GFP occupancy of each location	100%	28%	6%
Proportion of total Spir::GFP puncta at each location	57%	36%	7%

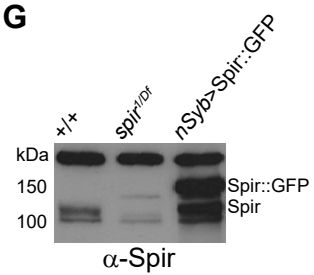

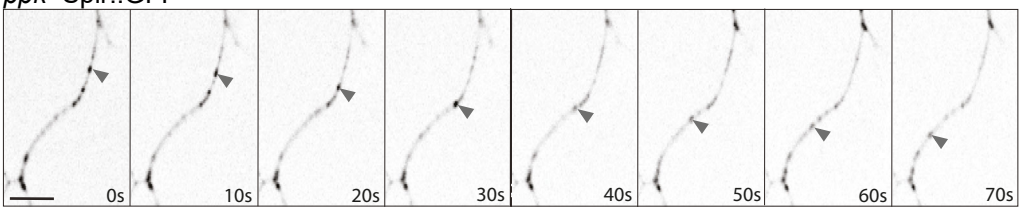

Figure S2

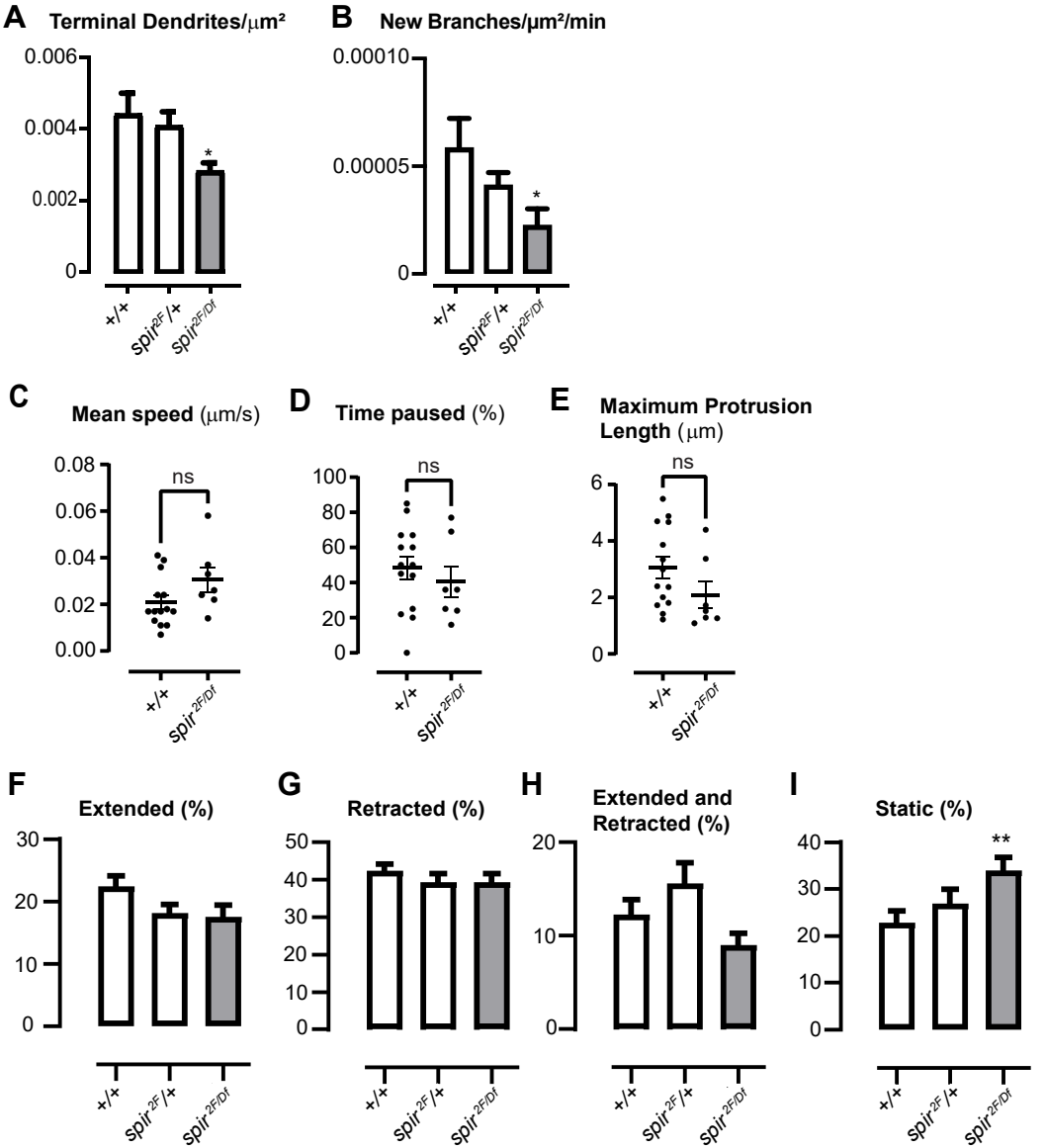
A
Terminal Dendrites/μm²
0.006
0.004
0.002
0
*
+/+
spir2F/+
spir2F/Df
B
New Branches/μm²/min
0.00010
0.00005
0
*
+/+
spir2F/+
spir2F/Df
C
Mean speed (μm/s)
0.08
0.06
0.04
0.02
0.00
ns
+/+
spir2F/Df
D
Time paused (%)
100
80
60
40
20
0
ns
+/+
spir2F/Df
E
Maximum Protrusion Length (μm)
6
4
2
0
ns
+/+
spir2F/Df
F
Extended (%)
30
20
10
0
+/+
spir2F/+
spir2F/Df
G
Retracted (%)
50
40
30
20
10
0
+/+
spir2F/+
spir2F/Df
H
Extended and Retracted (%)
20
10
0
+/+
spir2F/+
spir2F/Df
I
Static (%)
40
30
20
10
0
**
+/+
spir2F/+
spir2F/Df

Figure S3

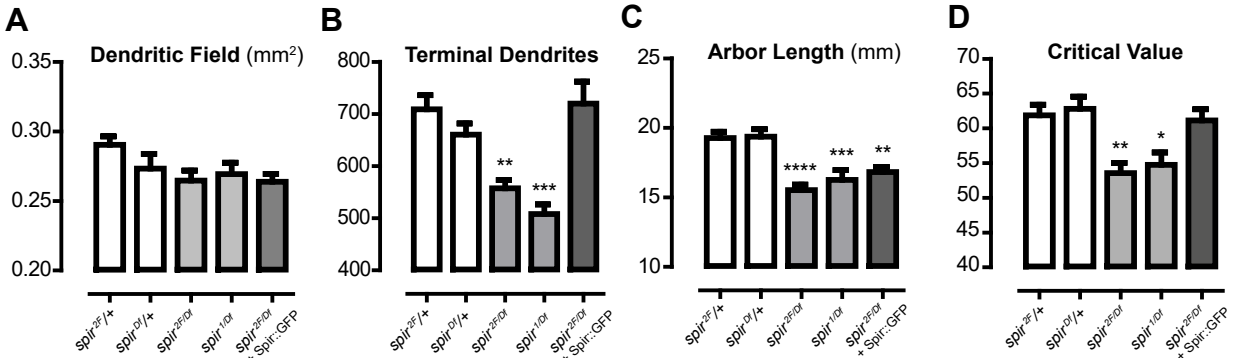
A
Dendritic Field (mm2)
0.35
0.30
0.25
0.20
B
Terminal Dendrites
800
700
600
500
400
**
***
C
Arbor Length (mm)
25
20
15
10
****
***
**
D
Critical Value
70
65
60
55
50
45
40
**
*
spir2F/+
spirD1/+
spir2F/Df
spir1/Df
spir2F/Df + Spir::GFP

Figure S4

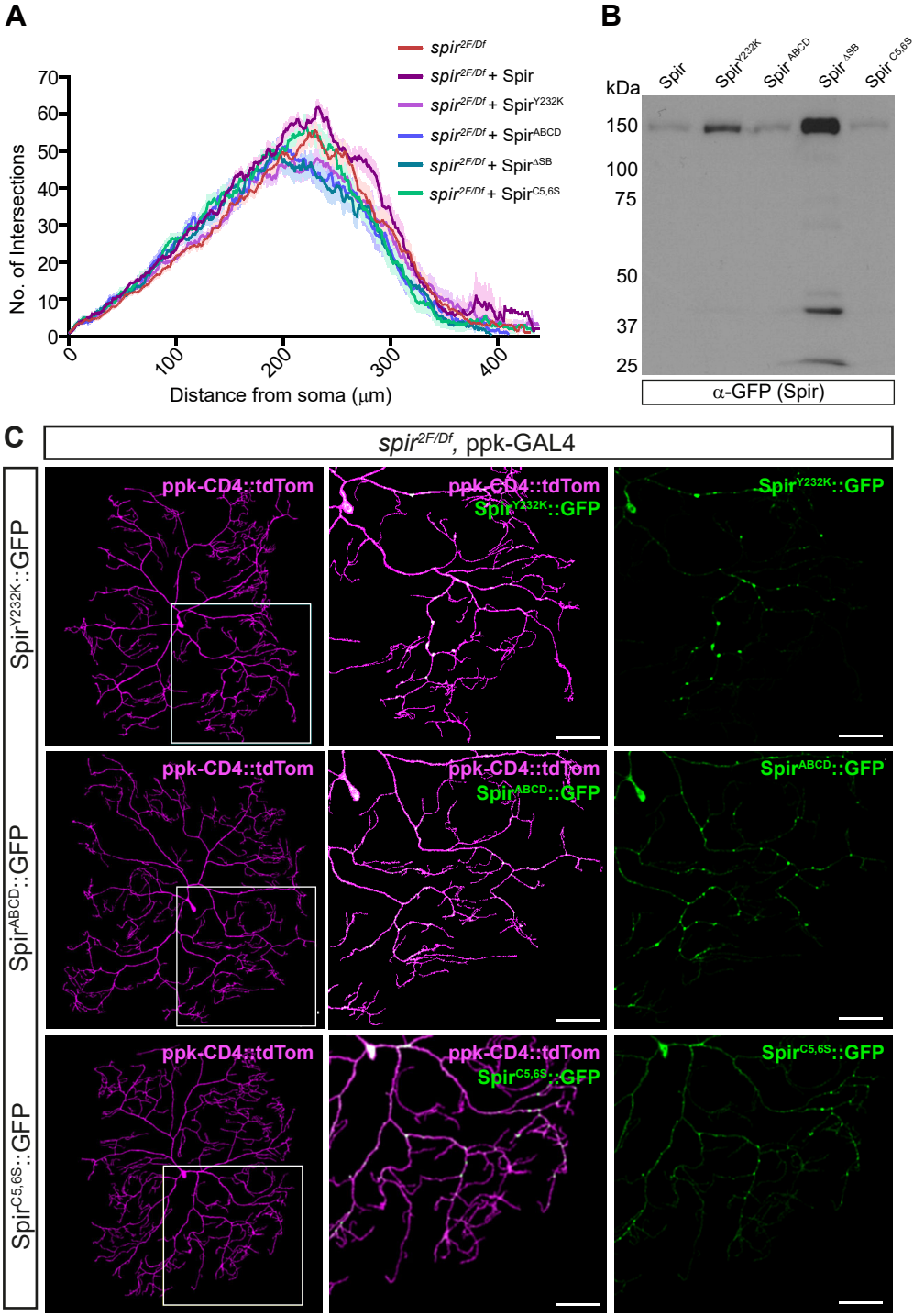
A
spir2F/Df
spir2F/Df + Spir
spir2F/Df + SpirY232K
spir2F/Df + SpirABCD
spir2F/Df + SpirΔSB
spir2F/Df + SpirC5,6S
No. of Intersections
Distance from soma (μm)
B
kDa
Spir
SpirY232K
SpirABCD
SpirΔSB
SpirC5,6S
150
100
75
50
37
25
α-GFP (Spir)
C
spir2F/Df, ppk-GAL4
SpirY232K::GFP
SpirABCD::GFP
SpirC5,6S::GFP
ppk-CD4::tdTom
ppk-CD4::tdTom SpirY232K::GFP
SpirY232K::GFP
ppk-CD4::tdTom SpirABCD::GFP
SpirABCD::GFP
ppk-CD4::tdTom SpirC5,6S::GFP
SpirC5,6S::GFP

Figure S5

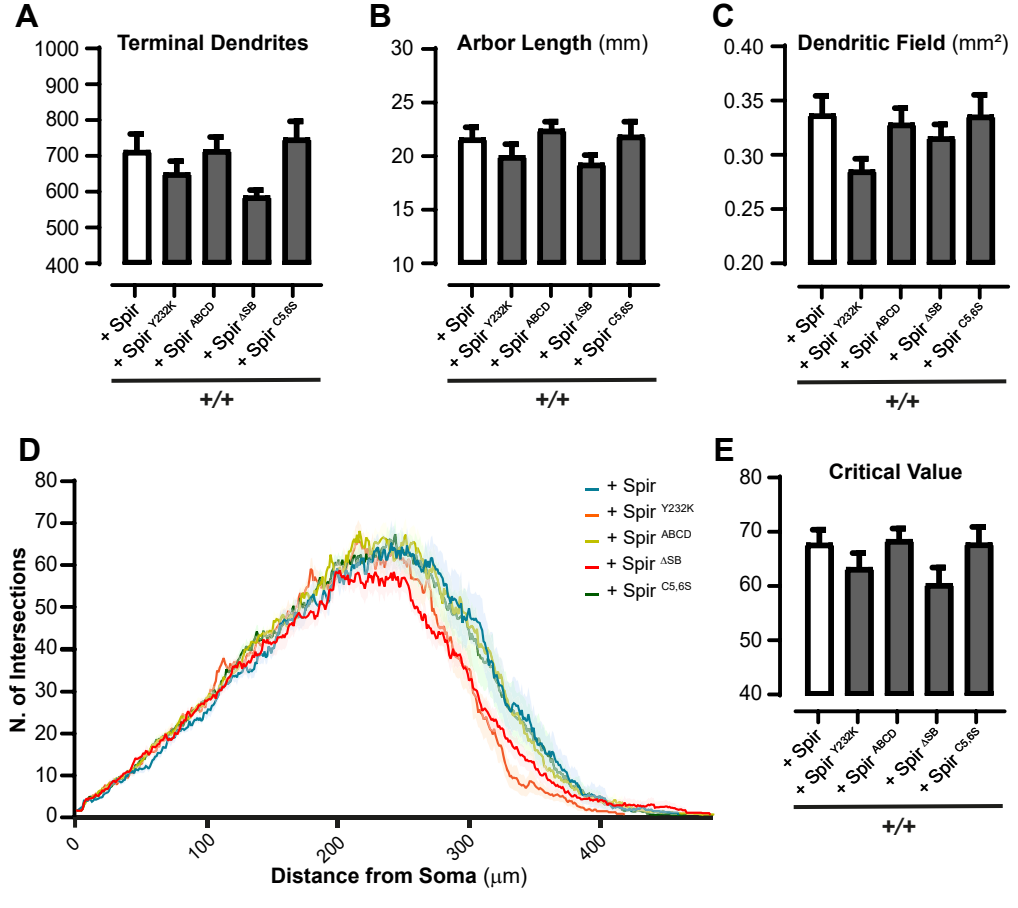
A
Terminal Dendrites
1000
900
800
700
600
500
400
+ Spir
+ Spir Y232K
+ Spir ABCD
+ Spir ΔSB
+ Spir C5,6S
+/+
B
Arbor Length (mm)
30
25
20
15
10
C
Dendritic Field (mm²)
0.40
0.35
0.30
0.25
0.20
D
N. of Intersections
80
70
60
50
40
30
20
10
0
0
100
200
300
400
Distance from Soma (μm)
E
Critical Value

Figure S6

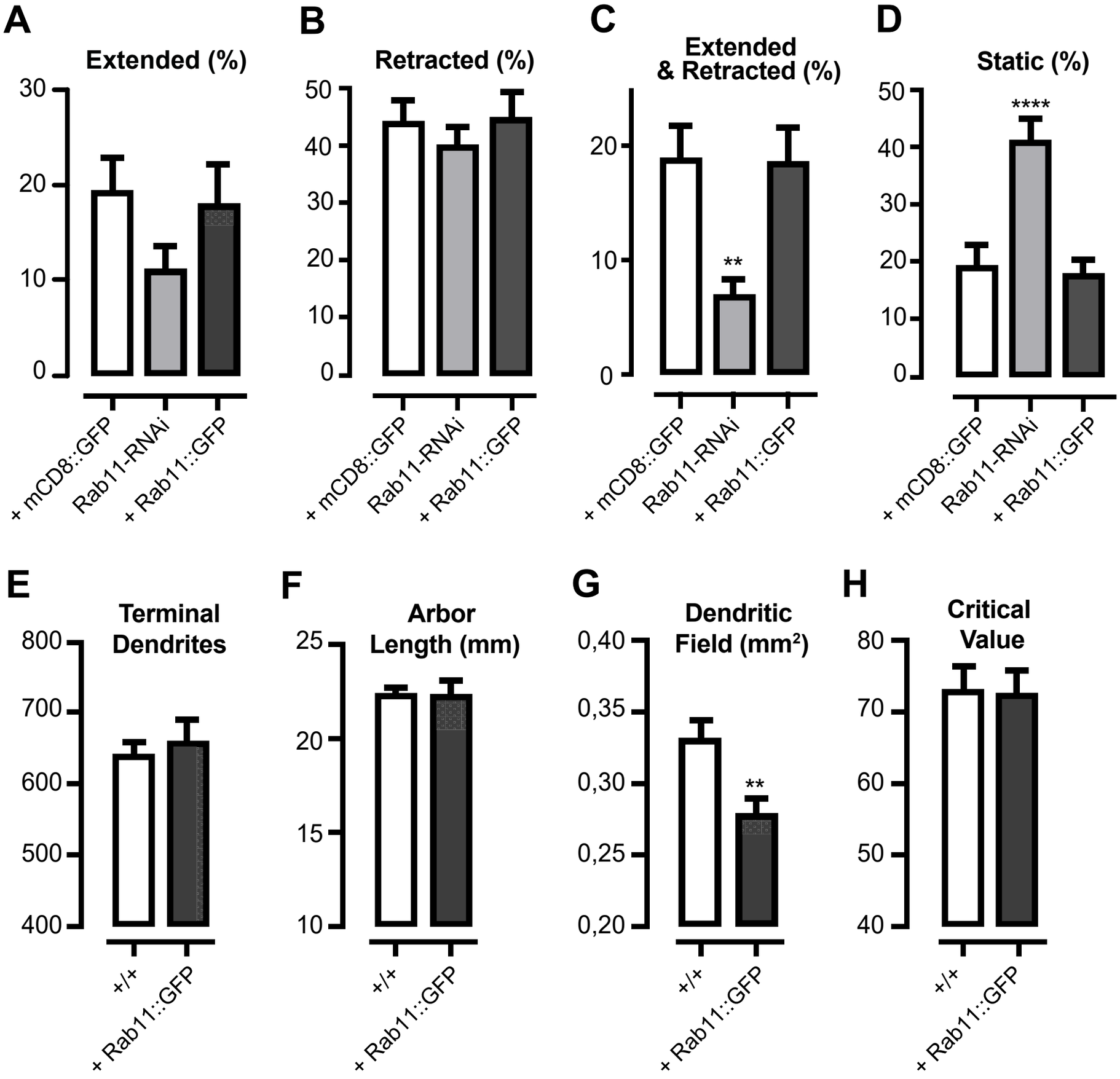
A
Extended (%)
30
20
10
0
+ mCD8::GFP
Rab11-RNAi
+ Rab11::GFP
B
Retracted (%)
50
40
30
20
10
0
+ mCD8::GFP
Rab11-RNAi
+ Rab11::GFP
C
Extended & Retracted (%)
20
10
0
**
+ mCD8::GFP
Rab11-RNAi
+ Rab11::GFP
D
Static (%)
50
40
30
20
10
0
****
+ mCD8::GFP
Rab11-RNAi
+ Rab11::GFP
E
Terminal Dendrites
800
700
600
500
400
+/+
+ Rab11::GFP
F
Arbor Length (mm)
25
20
15
10
+/+
+ Rab11::GFP
G
Dendritic Field (mm²)
0,40
0,35
0,30
0,25
0,20
**
+/+
+ Rab11::GFP
H
Critical Value
80
70
60
50
40
+/+
+ Rab11::GFP

Figure S7

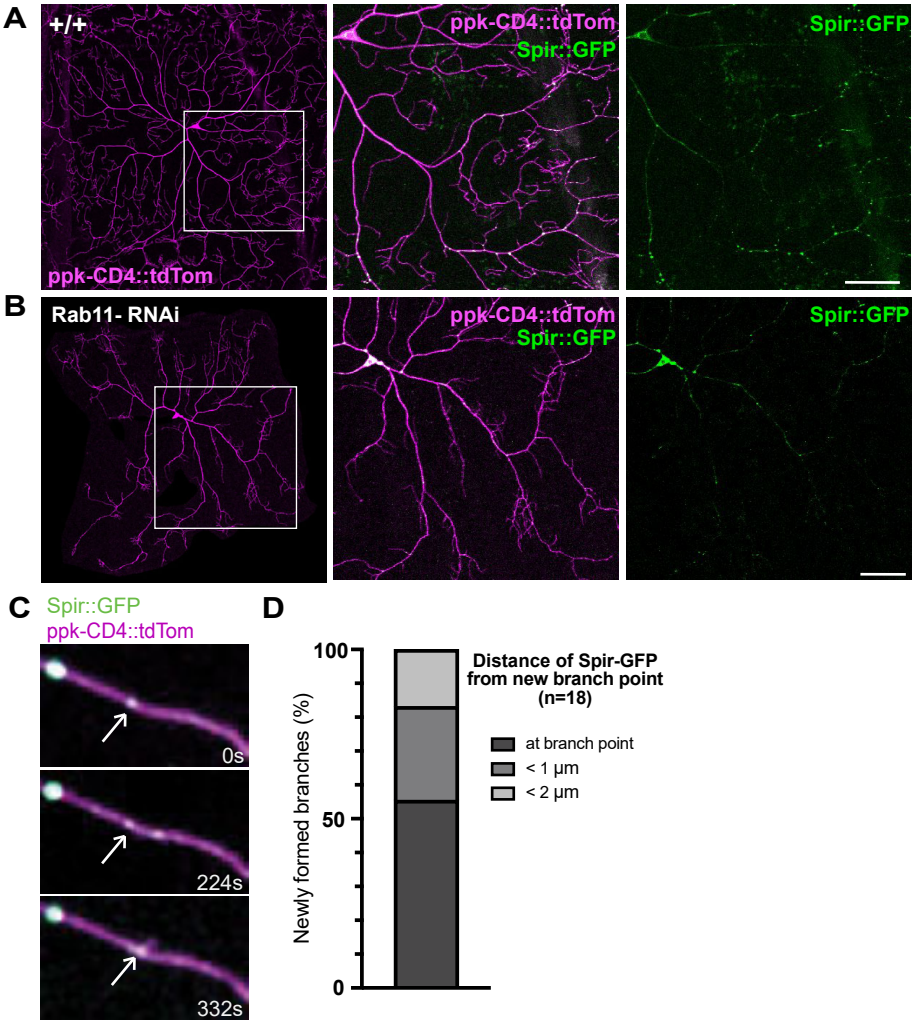
A
+/+
ppk-CD4::tdTom
ppk-CD4::tdTom
Spir::GFP
Spir::GFP
B
Rab11- RNAi
ppk-CD4::tdTom
Spir::GFP
Spir::GFP
C
Spir::GFP
ppk-CD4::tdTom
0s
224s
332s
D
Distance of Spir-GFP from new branch point (n=18)
at branch point
< 1 µm
< 2 µm
Newly formed branches (%)
100
50
0